

Application of Artificial Intelligence to Paper Based Colorimetric Sensors

Submitted to the Graduate School of Natural and Applied Sciences
in partial fulfillment of the requirements for the degree of

Master of Science

in Biomedical Engineering

by

Elif Yüzer

ORCID 0009-0003-5483-9442

July, 2023

This is to certify that we have read the thesis **Application of Artificial Intelligence to Paper Based Colorimetric Sensors** submitted by **Elif Yüzer**, and it has been judged to be successful, in scope and in quality, at the defense exam and accepted by our jury as a MASTER'S THESIS.

APPROVED BY:

Advisor: **Assoc. Prof. Dr. Mustafa Şen**
İzmir Kâtip Çelebi University

Co-advisor: **Assoc. Prof. Dr. Volkan Kılıç**
İzmir Kâtip Çelebi University

Committee Members:

Assoc. Prof. Dr. Mustafa Şen
Izmir Katip Celebi University

Assoc. Prof. Dr. Volkan Kılıç
İzmir Kâtip Çelebi University

Assoc. Prof. Dr. İlker Polatođlu
Celal Bayar University

Date of Defense: July 31, 2023

Declaration of Authorship

I, **Elif Yüzer**, declare that this thesis titled **Application of Artificial Intelligence to Paper Based Colorimetric Sensors** and the work presented in it are my own. I confirm that:

- This work was done wholly or mainly while in candidature for the Master's / Doctoral degree at this university.
- Where any part of this thesis has previously been submitted for a degree or any other qualification at this university or any other institution, this has been clearly stated.
- Where I have consulted the published work of others, this is always clearly attributed.
- Where I have quoted from the work of others, the source is always given. This thesis is entirely my own work, with the exception of such quotations.
- I have acknowledged all major sources of assistance.
- Where the thesis is based on work done by myself jointly with others, I have made clear exactly what was done by others and what I have contributed myself.

Date: 31.07.2023

Application of Artificial Intelligence to Paper Based Colorimetric Sensors

Abstract

Using color changes to measure the presence and concentration of the substance visible to the naked eye, colorimetric analysis is a method used in the detection of biomolecules. In many different industries, including the health, pharmaceutical, food, paint, and cosmetics sectors, the colorimetric analysis is used to analyze biological, medical, and environmental samples. Point-of-care (POC) tests are used in many areas due to their ease of use and accessibility. Integration of POC tests with colorimetric analysis increases ease of use. In colorimetric analysis, accurate measurement and calibration techniques are required to obtain accurate results. For this reason, artificial intelligence and smartphone technology have been widely used in the development of biological sensors in chemistry and biomedicine in recent years. Images obtained using a smartphone camera are processed with artificial intelligence techniques to obtain highly accurate results. In this thesis, lactate detection and H_2O_2 detection in sweat were performed using artificial intelligence approaches, respectively. First, H_2O_2 detection was performed using a Fe_3O_4 @chitosan nanozyme (Fe_3O_4 @chi) with a peroxidase-like activity using a μPAD . First, the catalytic performance of the Fe_3O_4 @Chi nanozyme was first evaluated by UV-Vis spectroscopy using 3,3',5,5'-tetramethylbenzidine. Unlike Fe_3O_4 nanoparticles (NP), Fe_3O_4 @Chi nanozyme exhibited an intrinsic peroxidase activity with a detection limit of 69 nM. Then, based on the reaction of the nanozyme with 3,3',5,5'-tetramethylbenzidine, colorimetric detection of H_2O_2 was performed with the help of a μPAD . A user-friendly system has been developed by integrating the system with an application called "Hi-perox

Sens++", which has machine learning classifiers. In the system where machine learning classifiers were trained using different light sources and different phone brands, images were taken at 30 seconds and 10 minutes. In the end, it was found that linear discriminant analysis had the highest classification accuracy (98.7%) with phone-independent repeatability at t=30 s, and accuracy was maintained for 10 minutes. Second, colorimetric detection of lactate was performed using horseradish peroxidase, lactate oxidase and 3,3',5,5'-tetramethylbenzidine reaction system to detect lactate in artificial sweat using a microfluidic paper-based analytical systems (μ PAD). Images obtained with different lighting conditions and different brands of phones were applied for the selective and quantitative analysis of lactate in sweat in a deep learning-based phone application called "DeepLactate". In the system where various deep learning models are trained, Inception-v3 with the highest performance is placed in the application. According to the results obtained, the current system showed 99.9% classification accuracy with phone-independent repeatability and a processing time of less than 1 second. A patch was then designed to detect lactate in human sweat on volunteers. Lactate detection was performed in volunteers after rest and exercise, respectively.

Keywords: Colorimetric Detection, Microfluidic Paper-based Analytical Systems, Non-Invasive Detection, 3,3',5,5'-tetramethylbenzidine, Artificial Intelligence, Smartphone App

Yapay Zekanın Kağıt Tabanlı Kolorimetrik Sensörlere Uygulanması

ÖZ

Kolorimetrik analiz, biyomoleküllerin saptanmasında kullanılan ve çıplak gözle gözlemlenen maddenin varlığını ve konsantrasyonunu belirlemek için renk değişimlerini kullanılarak ölçülmesini sağlayan bir tekniktir. Sağlık, gıda, ilaç, kozmetik ve boya endüstrileri gibi birçok farklı alanda biyolojik, tıbbi ve çevresel numunelerin analizinde kolorimetrik analiz kullanılmaktadır. Bakım-noktası (POC) testleri kullanım kolaylığı ve ulaşılabilirliği nedeniyle bir çok alanda kullanılmaktadır. POC testlerinin kolorimetrik analiz ile entegrasyonu kullanım kolaylığını arttırmaktadır. Kolorimetrik analizde, doğru sonuçlar elde etmek için doğru ölçüm ve kalibrasyon teknikleri gerekmektedir. Bu nedenle son yıllarda kimya ve biyotıpta biyolojik sensörlerin geliştirilmesinde yapay zeka ve akıllı telefon teknolojisi yaygın olarak kullanılmaktadır. Akıllı telefon kamerası kullanılarak elde edilen görüntüler, yapay zeka teknikleriyle işlenerek yüksek doğrulukta sonuçlar elde etmektedir. Bu tezde yapay zeka yaklaşımları kullanılarak sırasıyla terde laktat tespiti ve H₂O₂ tespiti gerçekleştirilmiştir. İlk olarak, bir μ PAD kullanılarak peroksidaz-benzeri aktivite gösteren bir Fe₃O₄@chitosan nanozim (Fe₃O₄@chi) kullanılarak H₂O₂ tespiti gerçekleştirilmiştir. Öncelikle, Fe₃O₄@Chi nanoziminin katalitik performansı ilk olarak 3,3',5,5'-tetrametilbenzidin kullanılarak UV-Vis spektroskopisi ile değerlendirildi. Fe₃O₄ nanoparçacıklarının (NP) aksine, Fe₃O₄@ Chi nanozim, 69 nM'lik bir tespit limiti ile içsel bir peroksidaz aktivitesi sergilemiştir. Ardından nanozimin 3,3',5,5'-tetrametilbenzidin ile reaksiyonuna dayanarak bir μ PAD yardımıyla H₂O₂'nin kolorimetrik tespiti gerçekleştirildi. Makine öğrenimi

sınıflandırıcılarak sahip "Hi-perox Sens++" adlı bir uygulama ile sistemin entegrasyonu gerçekleştirilerek kullanıcı dostu bir sistem geliştirilmiştir. Farklı ışık kaynakları ve farklı telefon markaları kullanılarak makine öğrenimi sınıflandırıcılarının eğitildiği sistemde 30. saniye ve 10. dakikalarda görüntüler alındı. Sonuçlara göre lineer diskriminant analizi, t=30 s'de telefonda bağımsız tekrarlanabilirlik ile en yüksek sınıflandırma doğruluğunu (%98,7) sergiledi ve doğruluk 10 dakika boyunca korundu. İkinci olarak, bir kağıt-tabanlı mikroakışkan cihaz (μ PAD) kullanılarak yapat terde laktat tespiti gerçekleştirmek amacıyla laktat oksidaz- yaban turpu peroksidazı ve 3,3',5,5' -tetramethylbenzidine reaksiyon sistemi kullanılarak laktatın kolorimetrik tespiti gerçekleştirilmiştir. Farklı aydınlatma koşulları ve farklı marka telefonlar ile elde edilen görüntüler "DeepLactate" adlı derin öğrenme tabanlı telefon uygulamasında terde ki laktatın seçici ve kantitatif analizi için uygulanmıştır. Çeşitli derin öğrenme modellerinin eğitildiği sistemde en yüksek performansa sahip Inception-v3 uygulama içerisine yerleştirilmiştir. Elde edilen sonuçlara göre, mevcut sistem telefonda bağımsız tekrarlanabilirliği ve 1 saniyeden kısa işlem süresi ile %99,9 sınıflandırma doğruluğu göstermiştir. Ardından gönüllüler üzerinde insan terinde laktat tespiti gerçekleştirmek amacıyla bir yama tasarlanmıştır. Sırasıyla dinlenme ve egzersiz sonrası gönüllülerde laktat tespiti gerçekleştirilmiştir.

Anahtar Kelimeler: Kolorimetrik Tespit, Mikroakışkan Kağıt Tabanlı Analitik Sistemler, İnvaziv Olmayan Tespit, 3,3',5,5' -tetrametilbenzidin, Yapay Zeka, Akıllı Telefon Uygulaması

To my family.

Acknowledgment

First of all, I would like to thank my advisor Assoc. Prof. Dr. Mustafa ŞEN for believing in me under all circumstances and always supporting me to achieve the best. I would especially like to thank him for developing me to reach my current researcher and personal personality. Thank him very much for guiding me to improve my skills and for always being kind.

I want to thank Assoc. Prof. Dr Volkan KILIÇ my co-advisor, significantly for his beneficial guidance and constructive comments, from which I gained great insights into my research.

I would like to thank İpek AVCI and Merve OĞUZ, who were my colleagues in the laboratory during my master's degree, for always supporting me and trying to help me when I had a problem.

I would like to thank my friends Aylin KORKMAZ, Alara ÖZGEN and Saadet DEMİRBAŞ for supporting me day and night during the process of preparing this thesis, for being with me during the times when I was in despair and for always making me feel their love.

Table of Contents

Declaration of Authorship.....	ii
Abstract.....	iii
Öz	v
Acknowledgment	viii
List of Figures	xii
List of Tables	xv
List of Abbreviations	xvi
List of Symbols	xix
1 Introduction	1
1.1 Biosensors.....	1
1.2 Optical Chemical/Biosensor.....	2
1.2.1 Fluorimetric sensors.....	4
1.2.2 Infrared sensors	5
1.2.3 Fiber-optic sensors.....	6
1.2.4 Colorimetric sensors	7
1.3 Microfluidic paper-based analytical systems (μ PADs).....	9
1.3.1 Fabrication of μ PADs.....	11
1.3.2 Colorimetric detection with μ PADs	13
1.4 Importance of non-invasive Detection	15
1.4.1 Hydrogen Peroxide.....	16

1.4.2	Lactate.....	17
1.5	Peroxidase-like activity of Nanoparticles.....	18
1.6	Artificial Intelligence in Colorimetry	19
1.7	Aim of Thesis.....	21
2	Colorimetric Detection of H ₂ O ₂ With Fe ₃ O ₄ @ Chi Nanozyme Modified μ pads Using Artificial Intelligence	22
2.1	Materials and Methods.....	22
2.1.1	Materials	22
2.1.2	Methods.....	22
2.1.2.1	Design and Fabrication of μ PAD	22
2.1.2.2	Synthesis and Characterization of Nanoparticles.....	23
2.1.2.3	Colorimetric Detections	23
2.1.2.4	Detection with UV-Vis	24
2.1.2.5	Image acquisition	25
2.1.2.6	Feature extraction and machine learning classifiers	26
2.1.2.7	Smartphone application: Hi-perox Sens++	27
2.1.2.8	Selectivity, Stability, and Real Sample Analysis	28
2.2	Results and Discussion.....	29
2.3	Conclusion.....	40
3	Smartphone Embedded Deep Learning Approach for Highly Accurate and Automated Colorimetric Lactate Analysis in Sweat	41
3.1	Materials and Methods.....	41
3.1.1	Materials	41

3.1.2	Methods.....	42
3.1.2.1	Design and Fabrication of μ PAD and Patch	42
3.1.2.2	Preparation of Artificial Sweat.....	42
3.1.2.3	Colorimetric Detections	43
3.1.2.4	Deep Learning.....	44
3.1.2.5	Image Acquisition.....	45
3.1.2.6	Smartphone app: DeepLactate	47
3.1.2.7	Selectivity, Stability, and Real Sample Analysis	48
3.2	Results and Discussion.....	49
3.3	Conclusion.....	54
	References	55
	Appendix A.....	74
	Appendix B.....	75
	Curriculum Vitae	76

List of Figures

Figure 1.1:Schematic Illustration of Optical Biosensors [10].....	3
Figure 1.2 :The working principle of fluorescent chemosensors [14]	4
Figure 1.3: Colorimetric detection of target DNA dependent on concentration [34] ..	7
Figure 1.4: Application area of μ PADs [40].....	10
Figure 1.5: Different type of μ PAD. μ PAD fabricated by wax printing (a). μ PAD fabricated by photolithography (b) [46].....	11
Figure 2.1: An illustration of the system's schematic. Images of the color change brought about by the oxidation of TMB by $\text{Fe}_3\text{O}_4@ \text{Chi}$ NPs at various H_2O_2 concentrations under seven different illuminations were taken using a smartphone camera.	24
Figure 2.2: The numerical values of the system created while capturing the photo are shown.	25
Figure 2.3: Demonstration of colorimetric H_2O_2 quantification procedures on the homepage of the Hi-perox Sens++. The gallery or smartphone camera can be used to select an image as shown in b. The selected image is displayed on the screen in c. The image is cropped using an adjustable crop box, and d displays the cropped area. The cropped patch is uploaded in e for H_2O_2 analysis. Finally, the result is given in f. ...	28

Figure 2.4: XRD (a) and FTIR (b) analysis results of Fe ₃ O ₄ @Chi NPs Fe ₃ O ₄ and Fe ₃ O ₄ .	30
Figure 2.5: Rietveld pattern analysis results and report of Fe ₃ O ₄ @Chi NPs.	30
Figure 2.6: DLS (a) and TGA (b) analysis results of Fe ₃ O ₄ @Chi NPs Fe ₃ O ₄ and Fe ₃ O ₄ .	30
Figure 2.7: Fe ₃ O ₄ @Chi NPs' time-dependent reaction to 200 μM of H ₂ O ₂ (a). A calibration curve showing the response of Fe ₃ O ₄ @Chi NPs in 0 to 1μM H ₂ O ₂ (n = 3).	31
Figure 2.8: UV-Vis spectra of TMB, Fe ₃ O ₄ , and Chi in 200 μM of H ₂ O ₂ (ai), as well as those of Fe ₃ O ₄ @Chi NPs in various concentrations of H ₂ O ₂ . A calibration curve showing the correlation between Fe ₃ O ₄ @Chi NP response and H ₂ O ₂ concentrations (n = 3) (aai). The visual color change of TMB, Fe ₃ O ₄ , Chi, and Fe ₃ O ₄ @ Chi NPs in solutions of H ₂ O ₂ at various concentrations (n = 3), and a comparison of their responses (bii). Fe ₃ O ₄ @ Chi NPs' effects on the color of μPADs that can be seen with the naked eye in the presence of TMB and various concentrations of H ₂ O ₂ as opposed to TMB only at 5000 μM of H ₂ O ₂ (c).	32
Figure 2.9: The effect of TMB (a) and Fe ₃ O ₄ @Chi (b) NPs on color intensity (t=10 min, n=3).	33
Figure 2.10: The effect of pH at 10 min.	33
Figure 2.11: The performance of LDA based on precision, recall, and F1-score at t = 30 s.	36
Figure 2.12: Evaluation of LDA with error bars in terms of precision, recall, and F1-score at t=10 min for Fe ₃ O ₄ @Chi	37
Figure 2.13: Confusion matrices of Fe ₃ O ₄ @ Chi NPs at t = 30 s (a) and t = 10 min (b) in various H ₂ O ₂ concentrations	37
Figure 2.14: Stability of the system for 8 days (n=3).	39

Figure 3.1: Images of μ PADs showing visually observable color changes with varying concentrations of lactate in artificial sweat at $t = 0$ min and $t = 5$ min. 43

Figure 3.2: A schematic illustration showing the working principle of the system. Lactate is first converted to pyruvate by LOx, releasing H_2O_2 which is then used by HRP for the oxidation of TMB. The color change is imaged using a smartphone camera and the lactate level is determined by DeepLactate, an app running deep learning classifier. 44

Figure 3.3: General structure of the CNN 45

Figure 3.4: The steps for colorimetric lactate analysis in DeepLactate are as follows. The home page of DeepLactate is given in (a). The user can select an image from the gallery in (b) or capture a new image using the smartphone camera. Then, after selecting the image from the gallery, the crop alert dialog is asked to the user as in (c). If the user taps the “NO” action, the result is calculated directly (without cropping) as shown in (d). Otherwise, the user is directed to the crop screen in (e), (f) and (h) when the “YES” action is tapped. The app is tested for the concentrations of 0 mM in (g) and 50 mM in (i). 48

Figure 3.5: An image (a) showing the application of a lactate patch for human sweat analysis. The patch was made by sandwiching a μ PAD between a sticking plaster and a transparent tape (bi-ii). Classification results of the smartphone app DeepLactate for lactate level in the sweat of two volunteers after resting and 15 min jogging. 49

Figure 3.6: Model Accuracy of Inception-v3 is given in (a) and Model Loss of Inception-v3 is shown in (b). 51

Figure 3.7: Confusion matrix of Inception-v3 in varying concentrations of the test dataset..... 52

Figure 3.8: ROC curves of Inception-v3 in varying concentrations of the test dataset. 53

Figure 3.9: Selectivity results based on intensity change (I). The intensity change was normalized by dividing the intensity at $t = 5$ min by the intensity at 0 min ($I_{t=5}/I_{t=0}$). 53

List of Tables

Table 2.1: Camera properties of the smartphones used for imaging.....	26
Table 2.2: Classification accuracy results for H ₂ O ₂ with different machine learning classifiers.....	34
Table 2.3: Evaluation of the LDA for Fe ₃ O ₄ @Chi at t=10 min in terms of precision, recall, and F1-score	36
Table 2.4: Determination of H ₂ O ₂ in tap water, synthetic serum and FBS based on the average of classification results.	39
Table 3.1: Camera properties of the smartphones used for imaging.....	46
Table 3.2: Experimental results of CNN models.	50

List of Abbreviations

Al ³⁺	Aluminum Ion
IgG	Immunoglobulin G
SWCNT	Single Walled Carbon Nanotube
SARS-CoV-2 virus	Severe Acute Respiratory Syndrome Coronavirus
UV-Vis	UV-Visible
AuNP	Gold Nanoparticle
TMB	3,3',5,5'-tetramethylbenzidine
Fe ₃ O ₄	Iron (III) Oxide
SA	Staphylococcus aureus
HRP	Horseradish-Peroxidase
LO _x	Lactate Oxidase
H ₂ O ₂	Hydrogen Peroxide
NH ₃	Ammonia
AgNO ₃	Silver Nanoparticle
AgNP	Silver Nanoparticle
μPADs	Microfluidic paper-based analytical systems
POC	Point-of-care
LOD	Limit of Detection
3D	3-Dimensional

2D	2-Dimensional
AKD	Alkyl ketene dimer
CO ₂	Carbon dioxide
PDMS	Polydimethylsiloxane
KI	Potassium Iodide
ROI	Region of Interest
ROS	Reactive Oxygen Species
LDH	Lactate Dehydrogenase
MLR	Multiple linear regression
HCA	Hierarchical clustering analysis
PCA	Principal component analysis
PLSDA	Partial least squares discriminant analysis
PCR	Principal component regression
RGB	Red-Green-Blue
CMYK	Cyan-Magenta-Yellow-Black
Lab	Lightness-Red-green-Blue-yellow
HSV	Hue-Saturation-Value
CIE	International Commission on Illumination
AI	Artificial Intelligence
ML	Machine Learning
DL	Deep Learning
c-ELISA	Enzyme-linked immunosorbent test
NaCl	Sodium Chloride
NaOH	Sodium Hydroxide
KCl	Potassium Chloride
CaCl ₂	Calcium Chloride
MgCl ₂	Magnesium Chloride

Na ₂ SO ₄	Sodium sulfate
NaHCO ₃	Sodium bicarbonate
FeCl ₂ .4H ₂ O	Iron (II) Chloride
FeCl ₃ .6H ₂ O	Iron (III) Chloride hexahydrate
HCl	Hydrochloric Acid
Chi	Chitosan
H ₂ O	Water
FBS	Fetal bovine serum
FTIR	Fourier-transform infrared spectroscopy
XRD	X-ray diffraction
DLS	Dynamic light scattering
LDA	Linear discriminant analysis
THz	Terahertz Radiation
CFU	Colony Forming Unit

List of Symbols

μmol	Micromole
mM	Millimole
L	Liter
mg	Milligram
ng	Nanogram
nm	Nanometer
dL	Deciliter
μg	Microgram
pM	Picomole
kg	Kilogramme
cm	Centimeter

Chapter 1

1 Introduction

1.1 Biosensors

Biosensors are analytical devices that produce signals for detecting or diagnosing a target analyte [1,2]. Selective or semi-quantitative analyses are performed using biological recognition elements like enzymes and antibodies to obtain a measurable signal with biosensors [3,4]. When biosensors are compared with traditional analytical devices, they have advantages such as speed, cost, unparalleled specificity, sensitivity, and on-site detection [1,2]. The components of biosensors are described in Clark's 1956 report, who is the father of biosensors. The electrode that measures the blood's oxygen content was used as the biosensor in this study [3,4]. Biosensors can be different shapes and different sizes for their intended use. In general, biosensors consist of five components which are bioreceptor, electronics, analyte, display, and transducer. The analyte is a component named the detected molecule. Biomolecules that recognize target substrates like enzymes, antibodies, or aptamers are named bioreceptor. Transducer is the equipment that converts the output signal produced as a result of the biochemical reaction into an electrical signal that can be processed. Electronics can be defined as converting electrical signal that converts that of transducers to digital forms. The display unit allows the users to read the response obtained. The evolution of biosensors is classified into three generations. It depends on the integration of bioreceptor into transducers. The earliest biosensors are unmediated amperometric biosensors that gauge analyte concentrations and the byproducts of bioreceptor reactions, which diffuse the surfaces of transducers and cause an electrical response. In second-generation biosensors, co-reactants and enzymes are integrated into the biological component layer to increase analytical

performance. In third and last-generation biosensors, electrode uses enzymes and mediators. In this generation of biosensors, electron transfers are used to establish direct interaction between the enzymes and electrode in place of intermediary processes [4]. Biosensors have some characteristics which are named stability, selectivity, linearity, sensitivity, response time, and reproducibility. These are the characteristics that are important to developing highly effective and capable biosensor systems. Selectivity is important for biosensors because bioreceptor has to recognize only its target analyte. In a mixture with different species and unwanted contaminants, a bioreceptor can recognize a target analyte. Stability is a vulnerability of a biosensor. The biosensor can be affected by environmental changes inside and outside of the biosensing device. In general meaning, stability is a degradation of the biosensor over time. Sensitivity is defined as the accurate determination of the amount of analyte at a minimum step and low concentration. Linearity gives an accuracy of the measured results because if the linearity is high concentration detection is higher. Response time describes as the time taken for 95% of results. Reproducibility is the capability of a biosensor's precision and accuracy. If the same sample with the biosensor gives the same results when measured more than once, it can be said to have reproducibility. Potential application areas of biosensors are listed as environment, biotechnology, and medicine. At the same time, biosensors have important requirements for their fertile usage. These requirements can be listed as output sensitivity, concentrations of required samples, concentrations measured analytes, time, re-usage of biosensors, and cleanliness of the system. Depending on the signal transmission methods, biosensors can be divided into different groups; optical, electrochemical, piezoelectric, thermometric and magnetic [4,5].

1.2 Optical Chemical/Biosensor

Optical biosensor presents more advantages than other analytical techniques. It is possible to detect chemical and biological matter in real-time, directly, with high sensitivity, stability, less noise, and immunity to external disturbance [5,6]. Small size and cost-effectiveness are other advantages when compared with conventional analytical methods. Besides that, one of the most effective sensors for cataloging affinity or catalytic receptors is optical biosensor technology [5,7]. Micro/nano-technologies, molecular biology, microelectronics, biotechnology, chemistry, and

microelectromechanical systems (MEMS) are among the many improved concepts and multidisciplinary approaches applied in the development of next-generation optical biosensors [5]. It is known that optical sensing is sensing that takes advantage of the interaction between biorecognition elements and the optical field. These biorecognition elements are antibodies, antigens, enzymes, nucleic acids, and cells. Optical biosensors are high-sensitivity and versatility devices that detect changes in the light property when the interaction between an analyte and a receptor. These properties can be absorption, light scattering, index of refraction, or fluorescence. Optical chemical sensors are the sensors that respond to optical signals or produce optical signals. When an analyte and a receptor interact, they respond to or produce optical signals. They provide real-time, fast, and very parameter sensing [5,7,8]. The optical biosensor uses these biorecognition elements to measure matter concentration and produces a proportional signal [5,7]. There are two types of optical biosensing: labeled and label-free based detection. When these two detection methods are compared, it becomes clear that the label-free detection method produces the signal as a direct result of the analyzed material interacting with the transducer. Due to its detection being more similar to its natural form, label-free detection is a simple and economical method [5,9]. Labeled-based detection uses a label for detection as the name suggests. The produced optical signal is produced with fluorescent, luminescent, or colorimetric methods [5]. In Figure 1.1 there is a schematic illustration of optical biosensors.

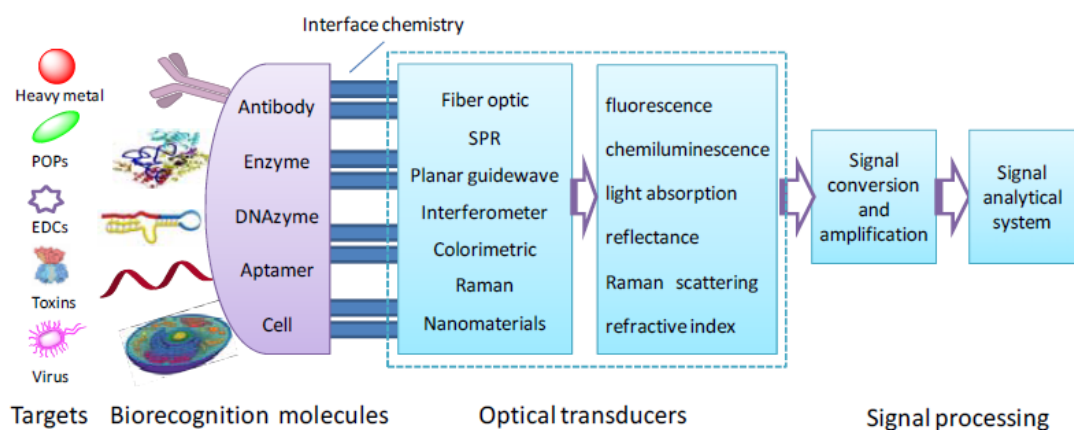


Figure 1.1: Schematic Illustration of Optical Biosensors [10].

1.2.1 Fluorimetric sensors

F. Goppelsroder first described fluorescent chemosensors in 1867 for the purpose of sensing the Al^{+3} ion. These devices are used for the selective detection of anionic and cationic species [11,12]. Fluorescence emission is started by forming an electronic excitation when light is absorbed from the fluorophore and it ends up light spread. After the excitation, the molecule absorbs light and stays excitation state. Subsequently, fluorescent emission is obtained with lower energy and higher wavelength than the excitation wavelength [13]. Fluorescent chemosensors, which are chemical types that use fluorescent properties to use measure electrical, thermal, magnetic, and electronic changes as well as optical changes, detect light using photodiodes or photomultipliers [14,15]. In the construction of fluorescent sensors, an intermediary component is in charge of the analyte's detection, and a signaling unit is in charge of the conversion of the measurable signal. The detection element is responsible for selectivity and binding productivity. The converter converts the information into an optical signal [13,14]. In the fluorescent chemosensor (Figure 1.2), generally, there are three main units. One of them is the receiving unit, which is in charge of selectively binding visitors, and the other is the species that are most likely to be impacted by the bonding event due to their optical properties. In some cases, there is a separator unit. This unit arranges electronic interaction between receptor and photoactive species [11].

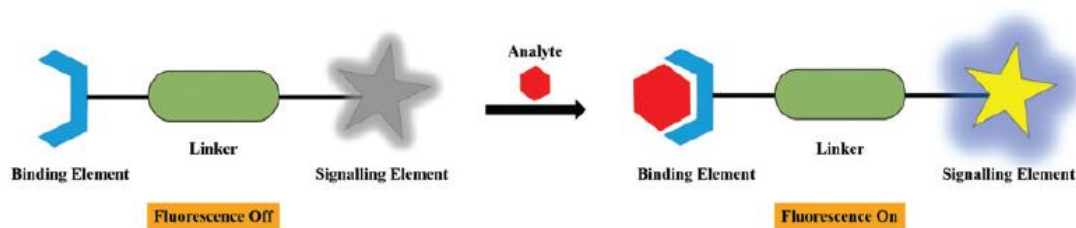


Figure 1.2 :The working principle of fluorescent chemosensors [14].

Instead of traditional methods like raman scattering, mass spectrometry, electrothermal atomic absorption spectrometry, voltammetry, and atomic absorption spectrometry fluorescent chemosensors are come to the forefront because of their high sensitivity, selectivity, naked-eye detection, cost-effectiveness, and low analyte concentration. In addition, it is advantageous to control the outputs by making changes in the molecular designs of the probes [11,14]. Due to the mechanical, electrical, and

optical properties of two-dimensional materials, it is widely used in the design of fluorescent biosensors. For example, carbon nanomaterials are highly preferred due to their stable and shiny structures [12,15].

In a study, a fluorescent method was used for the easy and high-sensitivity detection of glutathione. The results obtained showed that the limit of detection is 0.018 $\mu\text{mol/L}$ [16]. For the detection of 6-mercaptopurine used in cancer treatment, measurements were made using carbon quantum dots based on fluorescent emission. In this study, a detection limit of 0.001 mg/L was obtained [12]. In another study in the literature, the detection limit for chlorpyrifos, which was synthesized using a one-pot hydrothermal approach for the detection of pesticides, was found to be 2.7 ng/mL [17].

1.2.2 Infrared sensors

Infrared biosensors, like other biosensors, are a sensing technology that depends on the concentration of substances in biological samples. This type of sensor allows measurements to be taken using infrared spectroscopy methods. Near-infrared imaging in the range of 700-1700 nm, which is used as a non-invasive technique, is the most used in infrared sensors. This is brought on by their high signal-to-noise ratio, capacity for deep tissue penetration, and improved imaging resolution. NIR spectroscopy is a method that relates to vibrational and rotational transitions connected to chemical bonds within molecules and is used to determine the concentration of molecules by examining component bonds. This is due to the fact that biological tissues absorb and scatter NIR wavelengths less than visible ones [18–20].

A prototype of the near-infrared optical nose has been developed in a study in the literature. In this study, the optical properties of semiconductor single-walled carbon nanotubes were utilized [21].

In a study in the literature, graphene metasurface-based sensors were used to investigate infrared biosensors. The biosensor designed as a result of the experiments works in the infrared range of 250 THz–320 THz [22].

In a study published in the literature, it was investigated in the mid-infrared spectral range using biosensors based on metasurfaces that provide strong optical confinement

and tunable optical resonance. This study provided a highly sensitive and specific method for detecting the secondary structure of protein immunoglobulin (IgG) molecules [23].

A system that monitors blood glucose concentration with a wearable Vis-NIR-based biosensor has been developed for diabetics, which affects a large part of the world population. With the results obtained, the standard estimation error was found to be 6.16 mg/dL [19].

In another study in the literature, a paper-based NIR biosensor was developed to detect trypsin activity. Peptide-encapsulated SWCNTs were used for this detection. The lowest trypsin concentration detectable in this study was 1 $\mu\text{g/mL}$ [18].

1.2.3 Fiber-optic sensors

The fact that optical biosensors are disposable, not affected by electrical interference, and easy to miniaturize offers many advantages. The fact that fiber optic sensors are made of glass stands out because it increases resistance to ambient conditions and can be multiplexed on a single fiber network. In situations where conventional sensors cannot cope, fiber-optic sensors, which are immune to electromagnetic interference, are more convenient to use than other sensors. Since there is no electricity flowing at the sensing point, they are immune to electromagnetic interference. Because they are made of glass, they have a high tolerance for heat, shocks, and vibrations. Fiber-optic biosensors are made of filters and lenses, as well as optical components [24,25]. The development of lasers and modern low-cost optical fibers in the 1960s has greatly contributed to the development of fiber-optic sensors. The first developed chemical biosensors were made using low-loss fiber-optic sensors. In fiber-optic biosensors, the transmission of light is provided by a plastic optical fiber or silica glass fiber. These biosensors detect biomolecules by optical transduction mechanisms [24–26].

The total internal reflection principle determines how light travels through optical fibers. Thus, there is little environmental loss as light rays are directed through the fiber's core. Fiber-optic sensors can be used in conjunction with a variety of spectroscopic methods, including fluorescence, surface plasmon resonance, Raman,

and absorption. It is associated with the change in analyte concentration in the measurement that takes place in accordance with Beer's law [25].

The light emitted along the optical fiber consists of two components, the exponentially decreasing volatile field in the cladding and the guided one in the core. Light emitted in coated fibers with a uniform diameter does not interact with the surrounding of the fiber, since the lost area is reduced to almost zero within the coating [26]. Fiber-optic biosensors are divided into extrinsic and intrinsic sensors. Intrinsic sensors direct incoming and outgoing light based on volatile waves, while extrinsic sensors direct it with a bifurcated fiber or a single fiber [24].

A biosensor for the detection of some herbicides in *Chlorella vulgaris* cells was developed by Naessens et al. in the literature. Using kinetic measurements of chlorophyll-a fluorescence, the concentration of a toxic chemical was determined in this biosensor by placing microalgae in front of the end of the optic fiber bundle [27].

Murugan et al. have created a diagnostic platform based on a U-bent fiber optic sensor system for quick and early detection of the SARS-CoV-2 virus. Saliva can be used for plasmonic labeled and unlabeled immunoassays with the proposed plasmonic fiber optic absorbance biosensor [28].

1.2.4 Colorimetric sensors

Colorimetric analysis which is observed with the naked eye and used for the detection of biomolecules, stands out for manufacture and application of sensors and biosensors. This kind of detection method comes to the forefront when compared with other methods like electrochemical, electrophoresis, spectrometry, and chromatography because of fast, has no need for complicated tools, is low cost, has a simple detection mechanism, and is portable [29–33].

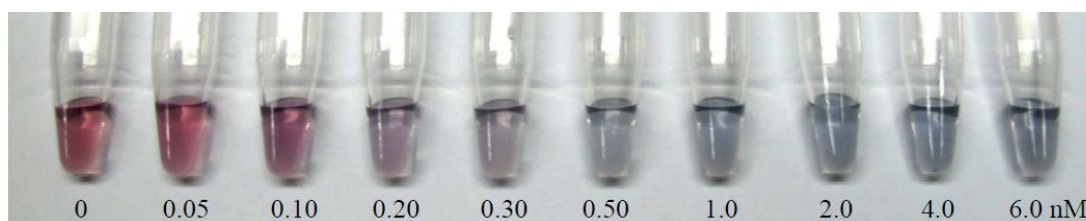


Figure 1.3: Colorimetric detection of target DNA dependent on concentration [34].

Visible color changes are obtained by using the concentration information in colorimetric detection. The main challenge in colorimetric detection is to convert the detection events into color changes [30,31].

In the fabrication of colorimetric sensors, functional materials or optical probes are used to obtain specific selectivity and colorimetric function. In the presence of biomolecular analytes, materials such as nanoparticles, polymers, carbon and graphene nanotubes, and metal nanoparticles can be used for sensing units. For colorimetric detection mechanisms, surface plasmon resonance, ligand-receptor binding, enzyme catalysis, nanozyme catalysis, color change of photonic crystals, and fluorescent on-off adjustment can be used depending on the materials that are used. [29,30,33]. When considering the fabrication and sensing properties these sensors can be used for the detection of viruses, heavy-metal ions, cells, DNA, small molecules, proteins, and other different chemicals [31,33].

Point-of-care (POC) tests are preferred for the diagnosis of diseases because of their time and cost savings properties. For POC tests that are suitable for daily use and do not require complex instrumentation and expertise, the application of the colorimetric method is more useful than other methods [29].

In the literature, developed a colorimetric sensor for detecting the concentration of *E.coli* bacteria with aggregation of gold nanoparticles (AuNP) has a lower detection limit of 50 CFU/mL. This sensor uses the blue-to-red color change of AuNP to detect bacterial concentration with smartphone imaging [35].

When salt concentration increases, AuNP aggregates and changes color from purple to blue. Based on this, Liu et.al designed a colorimetric sensor for DNA detection. The limit of detection of this sensor is 50 pM, and also the lower limit of naked eye detection was 100 pM [34].

For food safety purposes, the detection of two different mycotoxins using the catalysis of 3,3',5,5'-tetramethylbenzidine under acidic conditions was investigated. Zhu et.al fabricated a biosensor that combination of two colorimetric methods, for aflatoxins B1 detection $\text{Fe}_3\text{O}_4/\text{GO}$ and for ochratoxin A detection $\text{Fe}_3\text{O}_4@\text{Au}$ detection mechanisms used. The detection range of $5\text{-}250\text{ ng}\cdot\text{mL}^{-1}$ for aflatoxins B1 and $0.5\text{-}80\text{ ng}\cdot\text{mL}^{-1}$ for ochratoxin A was obtained [31].

In another study in the literature, colorimetric biosensor fabricated for the detection of *Staphylococcus aureus* (SA) take advantage of catalysis of specific aptamer and dsDNA-SYBR Green I (SG I) complex. The dsDNA-SG I complex generates an SA-sensitive photocatalyzed colorimetric response and catalyzes the oxidation of TMB under photo-irradiation. LOD of this colorimetric biosensor was obtained at 81 CFU mL⁻¹ [36].

Zeng et.al fabricated a colorimetric biosensor for fast and easy detection of cancer-derived exosomes with horseradish-peroxidase (HRP) encapsulated DNA nanoflowers. In this sensor, ABTS is oxidized in the presence of H₂O₂, and its color changes from colorless to green. The low detection limit was observed at 3.32 × 10³ particles/μL [37].

A POC colorimetric biosensor was developed for urea detection. In this sensor, hydrolysis of urea and urease to NH₃ was provided to take advantage of the reducing power of tannic acid, and colorimetric detection was performed as a result of silver nanoparticle (AgNP) production from AgNO₃. The limit of detection was obtained at 0,58 mM [29].

1.3 Microfluidic paper-based analytical systems (μPADs)

The use of paper in different areas is increasing day by day. Paper usage is preferred in the health and biomedical industry because of its unique properties. Figure 1.4 shows some applications of microfluidic paper-based analytical systems (μPADs). Thanks to the fibrous structure of the paper, chemicals are immobilized, and also, chemicals are stored because of absorbance. Another property is thanks to capillarity, transportation of liquid is easy. Air bubble formation is prevented thanks to its air permeability feature and thanks to the structure of the paper, liquids are filtered. Through the high surface/volume ratio, the number of reagents can be increased, thus reducing the analysis time. At the same time, the paper has high biocompatibility and biodegradability that encourages its use in the health and biomedical sector [38,39]. The things that encourage the use of paper in sensing devices are its advantages due to the above-mentioned properties. These advantages are; low cost, ease of access, fast

response, can be easily destroyed thanks to being flammable and does not require an external power for liquid transfer [39,40]. The use of paper in sensing devices first began in 1784 with litmus test papers for pH determination. For metal detection, spot tests were fabricated in the 1930s and 1940s [41]. After that, the detection of semi-quantitative urine-sugar [42], and blood sugar [43] devices were fabricated in the 1950s and 1970s.

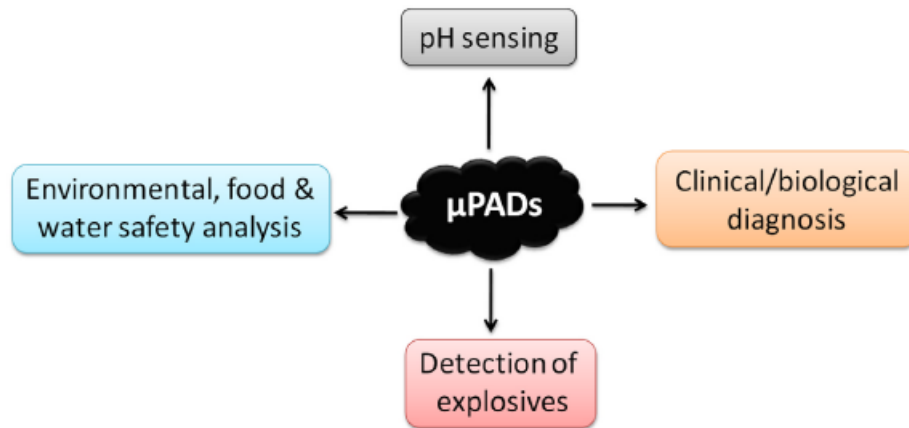


Figure 1.4: Application area of μ PADs [40].

Microfluidic technologies use for the analysis of biochemicals and medical diagnosis which was improved in 1979 by Terry et.al [44]. Materials for microfluidic technologies that use micron or submicron channels to detect liquid analytes include quartz and glass, monocrystalline crystalline silicon wafers, paper-based materials, and high molecular weight polymers [45].

The most important step for the treatment and prevention of disease is accurate and rapid diagnosis. The need for low-cost, fast-responding tests that do not require experienced personnel is increasing day by day. For this reason, Martinez et.al. introduced μ PADs in 2007 (Figure 1.5) [46]. μ PADs, which can be given as an example of the ASSURED statement determined by the World Health Organization, have the specified features. These qualities include affordability, accuracy, focus, friendliness, quickness, robustness, and ability to reach end users without the need for special equipment [45–47]. Providing the ASSURED principle, μ PADs are a widely used diagnostic device for point-of-care testing (POCT). POCT devices can be used in medical diagnosis as well as environmental monitoring, food safety, and where resources are limited. The most important advantages of μ PADs are the use of small

amounts of analyte and rapid diffusion, so their use in POCT devices draws attention. Other advantages of μ PADs are; It is easy to produce, user-friendly, environmentally friendly due to being made of paper, portable, and produce fast and simple analytical results [38–40,45–48].

In a study published in the literature, the colorimetric method with μ PAD was used to detect carcinoembryonic antigens. The obtained results indicated that the sensitivity was 98% and that the limit of detection (LOD) value was 0.015 ng/mL [49].

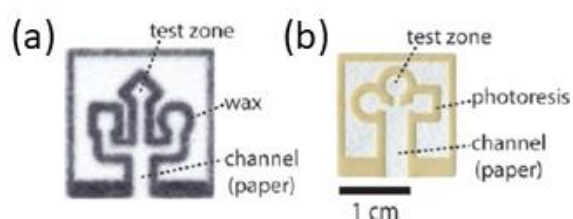


Figure 1.5: Different type of μ PAD. μ PAD fabricated by wax printing (a). μ PAD fabricated by photolithography (b) [46].

A μ PAD developed by Peters et al. has been developed for the detection of improvised explosives. 2 different μ PADs were designed and colorimetrically different explosives were detected. When the results were examined, the detection limit was obtained as 0.39-0.98 mg and the total analysis time was 5 minutes [50].

Ueland et al. carried out an investigation to identify explosive mixtures in soil using a combination of lab-on-a-chip and μ PAD for sample preparation and analysis. This combination, which has a minimum detectable amount range of 1.4-5.6 ng, is considered a viable approach due to its low cost per sample [51].

1.3.1 Fabrication of μ PADs

As a result of patterning the paper using various printing methods and hydrophobic inks, along with the identification of test regions and the use of hydrophobic barriers to delimit the hydrophilic channels, μ PADs are created. Indicating fluid penetration paths, hydrophobic barriers offer a very effective physical barrier to the paper. The patterns provided in the paper make it possible to perform multiple diagnostic tests while only using small volumes [52–54]. Both 3D and 2D formats can be used to

create μ PADs [55]. Wax printing, plotting, inkjet printing, laser cutting, flexographic printing, and photolithography methods can be used for production.

Wax printing: The benefits of choosing the wax printing technique are; It is cheap, environmentally friendly, and easy to produce. It is fast to manufacture and enables the production of many paper analytical instruments at once. For this method, there are three different approaches. Painting with a wax pencil is the first. This technique involves drawing the desired pattern on the paper with a wax pen, then heating the paper in an oven to melt the wax and seep it into the paper. The second method involves printing the computer-designed pattern on a regular printer, then passing it over with a wax pen and heating it in the oven. Utilizing a wax printer directly is the third and final strategy. This technique involves using a computer to draw the pattern, which is then taken out of the wax printer and heated in the oven. In these procedures, a heater or an oven is used to allow the wax to enter the paper and create defined microchannels on the paper [53,55–57]. There is a chance of contamination because the channels are open. Kevin and others have proposed a technique to create wax prints by using a printing toner on the top and bottom sides. Fully enclosed " μ PADs," made with beeswax and toner, were introduced in 2012. Wax was printed as hydrophobic barriers, and toner was printed as a seal on the top and bottom of the paper [56,57]. The main drawback of this approach is that most organic solvents do not work well with wax. Wax printing requires heating, and wax printers are scarce. In addition, the patterns' resolution is lower than it is for other approaches [55].

Inkjet printing: The inkjet printing process can be used to create paper-based microfluidic devices. This method makes it possible to precisely create zones for biological and chemical detection [53]. Alkyl ketene dimer (AKD) is the chemical of choice for hydrophobization in the paper. The AKD-heptane solution is printed on paper using an inkjet printing device, and the paper is then cured to the required level in the required amount of time to create hydrophobic barriers. Reduced cross-contamination, efficiency, high resolution, and quick fabrication are benefits of the method. The method is expensive, and organic solvents harm the device, which are drawbacks [57,58].

Photolithography: The first patterning technique was photolithography, which offers high sensitivity for the development of hydrophilic and hydrophobic areas on papers

[55]. The chromatography paper is first thoroughly coated with SU-8 photoresist before being baked. The photomask is then used to expose the paper to UV light. After a second baking of the paper, the non-polymerized photoresist is removed with acetone and allowed to dry. The paper is then treated with air plasma to create hydrophilic channels [57,58].

Laser-cutting: The process of laser cutting can be used to create μ PADs. In this method, the parchment paper is set up on a platform and cut to the desired shape using a CO₂ laser and computer control. In order to avoid damaging the paper during this process, laser power and scanning speed are crucial. Silica microparticles are applied to patterned areas to make the surface more wettable. In this technique, waxed paper can be used in place of parchment paper. Despite the method's low cost, it is not favored because of the pricey equipment required [56,58].

Plotting: For production, Whitesides et al. used x-y plotting. Polydimethylsiloxane (PDMS), a hydrophobic polymer that can dissolve, is used in this method. This solution was printed on filter paper using an x-y plotter to produce hydrophobic walls. It benefits from being inexpensive and physically adaptable. In this technique, the barrier thickness is also significant. A drawback arises if the barrier thickness cannot be controlled. [59].

Flexographic Printing: The flexographic printing process uses polystyrene. Using this method, polystyrene is deeply embedded in the filter paper. It consequently produces hydrophobic channels. Hydrophilic components are non-polystyrene parts. This approach holds promise for the large-scale manufacture of PADs. [60].

1.3.2 Colorimetric detection with μ PADs

Polymer-based materials can be used in analytical platforms using the microfluidic device although, since their use requires additional systems, they do not meet the ASSURED criteria. Therefore, using μ PADs is more advantageous. In μ PADs, where analysis can be performed with different methods, the colorimetric analysis step forth as it is not time-consuming and does not require complex equipment [61,62]. A visible color change in colorimetric analysis using μ PADs makes it easy to use and provides a user-friendly system. The biggest disadvantage encountered with this technology is

poor color uniformity. There are different techniques to overcome this problem. Some of these techniques are; paper oxidation, the addition of chitosan, and the control of fluid flow. In this way, the problem can be solved by obtaining color homogeneity [61].

In another research, a Griess reaction dependent μ PAD was developed for nitrite detection in pork. The analysis is completed within 15 minutes in μ PAD, which is integrated with a smartphone. In the analysis using the coffee-ring region, the linear regression range was obtained from 1 mg kg^{-1} to 250 mg*kg^{-1} and the LOD value was 1.1 mg*kg^{-1} [62].

In the research using 3 different combinations, a smartphone application using machine learning was developed for glucose detection. In this study, chitosan was added to one of the combinations to ensure color uniformity. In the study in which TMB and potassium iodide (KI) were used as chromogenic agents, an accuracy of 98.24% was obtained in the region of TMB [63].

In a research in the literature, colorimetric analysis was performed by creating hydrophobic channels using an adhesive stamp on a paper towel for the detection of glucose. The LOD value was calculated as $29.65 \mu\text{M}$ in the study using an offline smartphone application. In order to eliminate the disadvantage of poor color uniformity enabled precise extraction of ROI using Matlab and the application was tested with artificial saliva samples [61].

Colorimetric detection of C-reactive protein to determine heart disease risk was performed by Zheng et al using μ PAD. The detection performance of μ PADs was improved which was analyzed using machine learning. In the research using different classification models, ResNet gave the best results with 96% accuracy [64].

Sousa et al. performed the first dual μ PADs combined with a colorimetric and electrochemical module for POCT diagnosis of periodontal patients. In this study, salivary amylase, lactate, nitrite, and pH measurements were performed simultaneously. As a result of the experiments carried out with samples taken from sick and healthy individuals, it was observed that the amount of nitrite and salivary amylase was high in sick individuals. Almost no lactate detection was achieved in samples taken from sick individuals and acidic pH was observed [65].

1.4 Importance of non-invasive Detection

Early diagnosis, accurate and rapid detection, and monitoring of cell activity are very important for human health. Medical practitioner monitoring and self-monitoring are the two most common methods used today for health screening. There are two methods for performing health screenings. These are called invasive and non-invasive methods. The invasive method is a method that uses needles and the like to bore the human body for detection with blood but these procedures have a high risk of pain, suffering, and transmission of disease. Considering these disadvantages, non-invasive methods come to the fore. Introduced more than 30 years ago, non-invasive methods are diagnostics with fluids coming out of natural openings in the body. For example; sweat, urine, tears, and saliva are body fluids used in non-invasive diagnostic methods. It is drawing attention that non-invasive methods are an alternative to blood diagnostics. However, for the detection and diagnosis of biomolecules in the body, there must be a correlation between the amount of their presence in fluids such as sweat and urine and their amount in the blood. For this purpose, in which body fluid the molecule to be detected should be measured should be selected to be investigated [66–68].

The most useful method for non-invasive detection and health monitoring is sensor systems that are flexible, easy to use, and do not affect daily movements. Optical chemical sensors are preferred more than other sensor types because they provide real-time, fast results that do not require preliminary preparation [67,69]. The contents of the body fluids used in the measurement with the non-invasive method are important for the biomolecule to be determined as previously stated.

The tear is a biofluid that is secreted from lacrimal glands and contains various proteins [70], glucose [71], lysozyme [72], and ascorbic acid (AA) [73]. Sweat is secreted from sweat glands and they are categorized into two types of glands eccrine and apocrine. Minerals like magnesium and sodium, metabolites like lactate and urea, proteins, lipids, and steroids are among the substances found in sweat [74]. Saliva is a biological fluid that includes electrolytes, cations, enzymes, anions, hormones, lactate, proteins, urea, immunoglobulins, uric acid (UA), and immunoreactive insulin. Salivary glands are responsible for the secretion of saliva [75,76]. Urine is formed in

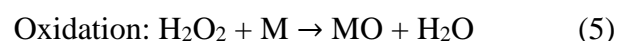
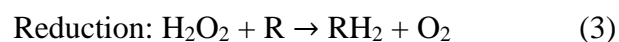
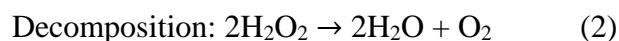
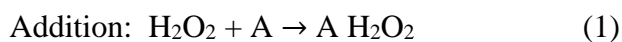
the kidneys and it is the filtration of blood. Components of urine are creatinine, ions such as chloride and potassium, urea, and uric acid [77].

Integration of wearable devices with non-invasive methods is very common. In a study conducted in the literature, a paper-based wearable system was designed and sweat lactate and pH measurements were carried out. The lactate sensor showed linear detection between 0-25 mM and the pH sensor between pH 4 and pH 8 [78].

A microfluidic paper-based sensor has been developed for the detection of COVID-19 disease by Bordbar et al. Colorimetric determination was made in this measurement taken by a non-invasive method. In their study, they used four different receptor groups to provide reliable responses between patients and healthy individuals. The sensitivity of the sensor for sick individuals was 73.3% [79].

1.4.1 Hydrogen Peroxide

Observing in 1818 that hydrogen peroxide is the product of the reaction of barium peroxide with nitric acid, Thenard also found that blood breaks down H_2O_2 . The world production of H_2O_2 , which is mainly used in the textile and paper industry [80] is over 2.2 Mton/year [81]. It is also used in pharmaceutical and medical applications [82]. There are reactions that hydrogen peroxide can undergo depending on the substrate type as molecular addition (Equation 1), decomposition (Equation 2), reduction (Equation 3), substitution (Equation 4), and oxidation (Equation 5) [81]. H_2O_2 , which is used as both an oxidant and a reducing agent, is preferred in many applications compared to other chemicals, as it gives environmentally friendly products, which are water and oxygen as side reaction products. It also has a high oxidation potential and is a versatile oxidant in the entire pH range with the water it produces as a by-product [81,83–85]. H_2O_2 is one of the most important representatives of reactive oxygen species (ROS) and is one of the responsible signaling molecules in different transmission processes such as disease progression or normal cell functions. H_2O_2 , which acts as a messenger molecule in cell shape changes, recruitment of immune cells, and initiation of cell proliferation, spreads between cells and tissues [83,85].



Due to all these features it has, H_2O_2 determination and monitoring are important in both environmental and medical diagnosis. It is particularly helpful in providing quantitative analysis of various enzyme substrates such as protein and carbohydrates [84,85]. Many different analytical techniques can be used for the determination of H_2O_2 . Examples of these methods can be colorimetry [86], titrimetry [87], chemiluminescence [88], and spectrophotometry [89].

In a study in the literature, an amperometric sensor was developed for the determination of H_2O_2 . In order to facilitate the reduction of H_2O_2 , nanoparticles were used in the study and a more understandable evaluation of the concentration ranges was achieved by using two different linear ranges [90].

A two-stage colorimetric system was used in a study by Zhang et al. to detect H_2O_2 . The outcomes demonstrated that the H_2O_2 detection limit was $0.3 \mu\text{M}$ [85].

1.4.2 Lactate

The two isomers of lactate, discovered by Carl Wilhelm Scheele in 1780 as a byproduct of milk, are L-lactate and D-lactate. L-lactate, generally produced in human cells, is almost 10 times more abundant than D-lactate in the blood. At the same time, L-lactate is a by-product that shows the transition from an aerobic state to an anaerobic state. Lactate dehydrogenase (LDH), the lactate oxidizing enzyme, is the byproduct of glycolysis and produces L-lactate as a result [91,92]. Both in the lab and at the point of care, L-lactate is measured [92]. It has also gained importance in the fermentation and dairy industry [93]. L-lactate, which is the carbon source for the synthesis of various biomolecules, is a biomarker in energy metabolism [94].

It is known that lactate is important in evaluating physical performance in military, sports, and health applications, as it is an important marker in tissue oxygenation and shock/trauma treatment. The normal lactate level in human blood is between 0.5-1.5 mM and it can be increased to 25 mM in excessive activity and certain medical conditions [95]. In a healthy person sweat lactate concentration is between 10-25 mM. At the same time, lactate is found in interstitial fluid, saliva, and tear, and the concentration of lactate is between 1.9-2.2 mM, 0.1-2.5 mM, and 1-5 mM respectively [96]. When physical activity is intense, aerobic metabolism is insufficient. In this case, glycogen stored in the muscles is used for energy and lactate production. Due to these features, lactate must be followed by health personnel and trainers in cases where high performance is required [74,91,97].

In a study by Jia et al., lactate from human sweat was measured for the first time in real-time using an electrochemical biosensor. A flexible printed temporary transfer tattoo serves as the sensor that is measured while exercising. Lactate was measured by this enzyme sensor linearly up to 20 mM [98].

In another study in the literature, sweat lactate measurement was performed. In this study, a design that can be easily adhered to the skin using a paper-based sensor was used. A low detection limit of 0.06 mM was obtained in this biosensor, which is a disposable wearable analytical platform [99].

1.5 Peroxidase-like activity of Nanoparticles

Their size-dependent physical and chemical properties make nanoparticles stand out in many areas. Combining the properties of solids with the ability of molecules to move, nanoparticles form large surfaces that can interact with biological systems due to their small size [100,101]. An important advantage of nanoparticles is that they can be imparted with various metal and semiconductor core materials such as magnetic and fluorescence behaviors [102].

Enzymes, one of the basic macromolecules, have an important place in the field of biomedicine because they can catalyze biological systems and have high selectivity. However, due to their disadvantages [103] (expensive, easily degraded, difficult storage conditions, etc.), different materials that can replace them have been

researched for a long time. For this purpose, man-made nanomaterials that can replace enzymes have been produced. Nanoparticles called nanozymes, which replace enzymes and are preferred due to their particle sizes [104], shapes, and structures [105] are used in the field of biosensing. The large surface-to-volume ratio, high catalytic activity, high surface reaction activity, and strong adsorption properties of these nanoparticles provide great advantages for biosensor applications [106–110]. Particularly in biosensor studies, nanoparticles with peroxidase activity draw attention. In 2007, Fe₃O₄ nanoparticles are the first original nanozyme imitating peroxidase activity in the literature [111].

Carbon nanoparticles (PtCNPs) coated with Pt have been used to create a biosensor that can detect glucose. In this experiment, H₂O₂ and PtCNPs catalyze TMB in place of HRP. According to the results, the detection limit for glucose is 0.30 mM and for H₂O₂ is 0.15 mM [108].

A point-of-care test based on the peroxidase activity of Au@Pt nanoparticles was carried out for the quick and precise detection of severe acute respiratory syndrome coronavirus 2 (SARS-CoV-2). The LOD was 11 ng mL⁻¹ in the study conducted for the colorimetric detection of the spike (S1) protein of SARS-CoV-2 [112].

1.6 Artificial Intelligence in Colorimetry

The biggest disadvantages in colorimetric analysis are environmental conditions and camera optics. In order to eliminate these disadvantages, artificial intelligence approaches in the quantitative evaluation process have become a trend recently. Chemometrics is the use of mathematical or statistical methods to design or choose the best experiments and measurement techniques and to query the most chemical information by examining chemical data. Principal component analysis (PCA), multiple linear regression (MLR), hierarchical clustering analysis (HCA), principal component regression (PCR), partial least squares discriminant analysis (PLSDA), and their combinations are the most frequently used chemometric techniques [1,63,113]. The purpose of using color spaces in colorimetric analysis is to measure and describe the colors produced by a sample. Commonly used color spaces in the colorimetric analysis are L*a*b*, RGB, HSV, CMYK, and CIE Lab*. The color space

used to measure color differences and used independently of the device is $L^*a^*b^*$. Defines colors by their L-value or their lightness. It also defines it according to the red-green and blue-yellow color components [114]. An additional color space that describes the colors produced by digital displays is RGB. It describes colors based on the red, green, and blue light required to produce a particular color [115]. Used in CMYK printing as a subtractive color space [116]. Another color space used in colorimetric analysis is CIE Lab* defined by the International Commission on Illumination (CIE). This color space is similar to the Lab color space. The difference from the Lab color space is that it is based on a standard observer model [117].

The disadvantages of the calibration curve used in colorimetric sensors encourage the use of artificial intelligence (AI) approaches. AI algorithms (Machine Learning (ML) and Deep Learning (DL)) can quickly and accurately measure the concentration of the substance. ML and DL algorithms can be trained to recognize patterns in colorimetric data and use that information to measure the concentration of a particular substance in a sample. The advantages of artificial intelligence algorithms in colorimetric analysis can be sorted; increased accuracy, fast results, automation, optimization, detection of complex models, and integration [118,119].

The use of smartphones in colorimetric analysis is particularly noteworthy for POC tests. It can be used to find the concentration of molecules by analyzing the RGB values of the color change in the image obtained with the smartphone camera. The main advantages of using smartphones as a colorimeter can be sorted; low cost, integration with applications, portability, user-friendly system, and high-quality imaging [63,120].

A machine learning-based smartphone application was developed to detect H_2O_2 . Images are processed for feature extraction to eliminate camera optics issues. Then, in the study using machine learning, the highest classification accuracy was obtained with a repeatability of 97.8% [120].

In another study in the literature, a deep learning-based smartphone application was developed using the enzyme-linked immunosorbent test (c-ELISA). In the study using μ PAD, an accuracy of over 97% was achieved in the classification of the results [121].

1.7 Aim of Thesis

This project, it is aimed to perform a colorimetric analysis of quantitative data obtained from images photographed with a smartphone camera using artificial intelligence methods. This thesis aimed to change the color of the solution depending on the lactate concentration with a deep learning-based smartphone application, and the change of the hydrogen peroxide concentration using nanoparticles with peroxidase-mimetic activity, with a machine learning-based smartphone application. At the same time, this kit is aimed to be easy to use for non-professionals. Chapter 2, it is aimed to detect H_2O_2 concentration with peroxidase-mimetic activity magnetic NPs and use a machine learning-based smartphone application. It is aimed to detect the lactate concentration in sweat with a smartphone application developed using deep learning in Chapter 3. It is aimed to produce a colorimetric analysis kit for the clinic by integrating a colorimetric analysis-based microfluidic analytical device (μ PAD) and a smartphone application for use in sports medicine.

Chapter 2

2 Colorimetric Detection of H₂O₂ With Fe₃O₄@ Chi Nanozyme Modified μ pads Using Artificial Intelligence

2.1 Materials and Methods

2.1.1 Materials

TMB, H₂O₂ (≥ 30 wt%), Chi – high molecular weight, acetic acid ($\geq 99\%$), D(+)-glucose ($\geq 99.5\%$), sucrose ($\geq 99.5\%$), lactic acid ($\geq 85\%$), urea ($\geq 99.5\%$), KCl ($\geq 99\%$), NaCl ($\geq 99.5\%$), CaCl₂ ($\geq 93\%$), MgCl₂ ($\geq 98\%$), Na₂SO₄ ($\geq 99\%$), NaHCO₃ ($\geq 99.7\%$), FeCl₂.4H₂O ($\geq 99.0\%$) FeCl₃.6H₂O ($\geq 99.0\%$), NaOH ($\geq 97.0\%$), HCl (37 wt%), and fetal bovine serum (FBS). All chemicals were supplied by Sigma- Aldrich, USA. Synthetic serum (physiologic) (Osel, Turkey). Whatman qualitative filter paper – grade 1 (Sigma-Aldrich, USA).

2.1.2 Methods

2.1.2.1 Design and Fabrication of μ PAD

First, the Microsoft PowerPoint program was used to create a design for the μ PADs. The design was then printed using a Wax printer (ColorQube 8900 Multifunction Printer, Xerox, USA) on Whatman filter paper. Whatman No. 1 filter paper is the material used for the production of μ PADs. μ PADs were made in the shape of a circle,

with an outer diameter of 0.6 cm and an inner diameter of 0.4 cm. The filter paper was then placed on a hot plate for 3–4 minutes at 120 °C to speed up the diffusion of the solid ink into the paper's pores and create the hydrophobic barriers.

2.1.2.2 Synthesis and Characterization of Nanoparticles

Co-precipitation of 1.72 g of Fe (II) and 4.7 g of Fe (III) salts in 50 mL dH₂O produced Fe₃O₄ NPs. The iron salt solution was then added 3 M of ammonia at a rate of 10 mL per minute while being mechanically stirred. A black precipitate was finally produced after the process was continued until the pH level reached 10. Fe₃O₄ NPs were then washed with dH₂O to remove alkali metals and bring the pH level to a neutral range (pH ±7). After that, samples were freeze-dried for characterization and storage. Fe₃O₄@Chi NPs were subsequently created. In simple terms, high molecular weight Chi was dissolved in 1 M acetic acid solution to produce 0.2 mg mL⁻¹ of Chi solution. Then, 100 mL of Chi solution was added, along with 70 mg of Fe₃O₄, and the mixture was mixed for 18 hours. In essence, during this process, Chi was adsorbed on the NP surface, resulting in a uniform dark brown suspension. Using a magnet and water, the magnetic Fe₃O₄@Chi NPs were washed numerous times. To confirm the functional groups on their surfaces, Fe₃O₄ and Fe₃O₄@Chi NPs performed Fourier-transform infrared spectroscopy (FTIR) measurements. Then, an X-ray diffractometer was used to characterize the iron phase abundance, morphology, crystallite size, and magnetic properties of both NPs. The patterns from X-ray diffraction (XRD) were subjected to Rietveld pattern analysis. Their particle size distribution was also measured using dynamic light scattering (DLS). Using a thermogravimetric system (TGA-SDT Q600 analyzer, TA Instruments, USA), the thermal characteristics of the Fe₃O₄@ Chi NPs were investigated. The sample was first put into an alumina crucible with 4 mg for analysis. The temperature was then increased by 20 °C per minute until it reached 600 °C.

2.1.2.3 Colorimetric Detections

For colorimetric detection, 0.8 and 1 µL of Fe₃O₄@Chi NPs were added to the detection zones, respectively. After each addition, the PADs were allowed to air-dry at room temperature. After that, H₂O₂ solutions of varying concentrations (0.01 mM,

0.05 mM, 0.1 mM, 0.2 mM, 0.5 mM, 1 mM, 5 mM, 10 mM, 25 mM, 50 mM) were used to test the PADs. A smartphone was used to image the color change obtained at $t = 30$ s and $t = 10$ min for each concentration level after 2 μ L aliquots of H_2O_2 solutions were added to the detection areas of the μ PADs (Figure 2.1).

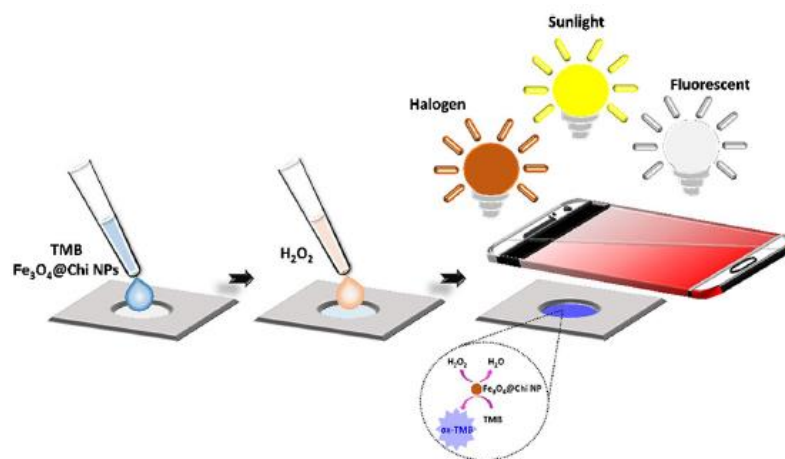


Figure 2.1: An illustration of the system's schematic. Images of the color change brought about by the oxidation of TMB by $\text{Fe}_3\text{O}_4@$ Chi NPs at various H_2O_2 concentrations under seven different illuminations were taken using a smartphone camera.

2.1.2.4 Detection with UV-Vis

TMB and H_2O_2 solutions were prepared in ethanol and dH_2O , respectively. Time-dependent absorbance of $\text{Fe}_3\text{O}_4@$ Chi NPs was recorded every 4 s at 645 nm for 300 s in a mixture containing 50 μ L of TMB, 50 μ L of 2 mg mL^{-1} $\text{Fe}_3\text{O}_4@$ Chi NPs, and 900 μ L of 200 μ M H_2O_2 . The absorption spectrum was recorded by UV-Vis spectrophotometer in a quartz cuvette with a 1 cm path length (Evolution 201/220, Thermo Scientific, USA). Next, H_2O_2 concentration-dependent absorbance was obtained at 120 s by adding H_2O_2 at varying concentrations (0, 0.25, 0.5, 1, 10, 20, 50, 100, and 200 μ M) to the mixture. For comparison, the impact of Fe_3O_4 NPs, TMB, and Chi on color change was investigated with 200 μ M of H_2O_2 simply by recording the UV-Vis spectra at 120 s. Fe_3O_4 NPs and Chi were tested in the same way as $\text{Fe}_3\text{O}_4@$ Chi NPs, where a mixture containing 50 μ L TMB and 900 μ L of 200 μ M H_2O_2 was mixed with 50 μ L 2 mg mL^{-1} Fe_3O_4 NPs and 1% (w/v) Chi in acetic acid, 2% (v/v), respectively. To investigate the impact of TMB alone on color change, 50 μ L TMB was mixed with 50 μ L of dH_2O and 900 μ L of 200 μ M H_2O_2 .

2.1.2.5 Image acquisition

The acquisition of images is a key step in enhancing the machine learning classifiers' resilience to challenging circumstances like ambient light and camera optics [63,120]. A dataset for training classifiers must mimic every scenario in order for them to function with phone-independent repeatability under a variety of lighting conditions [122,123]. In order to ensure that the dataset was large enough to handle the challenging circumstances, images were taken with multiple smartphones under controlled lighting conditions, including halogen (H), fluorescent (F), and sunlight (S) bulb sources. H (Osram 60 W), F (Klite 6 W), and S (Philips 5.5 W) light bulb sources were purposefully selected with various characteristics as hot (2700 K), neutral (4000 K), and cold (6500 K), respectively. The dataset could be expanded by using additional illumination sources, but three sources were found to be adequate because seven lighting conditions (H, F, S, HF, HS, FS, and HFS) were obtained by combining the light sources in different ways. Images of μ PADs were taken with a smartphone at a distance of 8 cm and a 30° incident angle. Additionally, the distances between the H, F, and S lamp sources and the PADs were 50, 53, and 57 cm, respectively. (Figure 2.2).

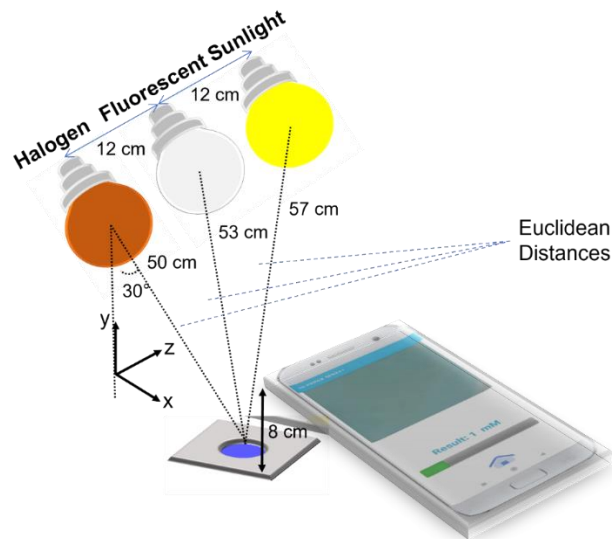


Figure 2.2: The numerical values of the system created while capturing the photo are shown.

To ensure phone-independent repeatability, the setup uses four different smartphones (iPhone 6S, iPhone 5SE, Oppo A5 2020, and Reeder P10) running Android and iOS and with distinctive camera properties (Table 2.1). The shutter speed, ISO, exposure time, and color temperature were all adjusted by the embedded imaging software while using a smartphone camera in auto mode. At $t = 30$ s and $t = 10$ min intervals, PAD images with eight different concentration values were captured, yielding 448 images for the dataset. The dataset was uploaded to a computer and used in the MATLAB (MathWorks, MA, USA) environment to extract the features from these images.

Table 2.1: Camera properties of the smartphones used for imaging.

Smartphone	Image	Optics	Camera
brand	resolution		resolution
Oppo A5 2020	4000 x 3000	f/1.8	12 MP
iPhone 5SE	4032 x 3024	f/2.2	12 MP
iPhone 6S	4032 x 3024	f/2.2	12 MP
Reeder P10	4160 x 3120	f/2	13 MP

2.1.2.6 Feature extraction and machine learning classifiers

Feature extraction derives a new input representation with reduced dimensions containing informative and nonredundant sets of feature vectors [63]. Extracted features are important because, during the training phase, classifiers learn to distinguish inputs based on them. Therefore, more distinguishing features enable classifiers to precisely differentiate between inputs. As they are promising in terms of image representation, color and texture information are used in this study to extract the image features [120]. The region of interest (ROI) was cropped to obtain the color channels R, G, B, H, S, V, L^* , a^* , and b^* after converting the RGB image to HSV and $L^*a^*b^*$ for each concentration. Then, values for each color channel's mean, skewness, and kurtosis were determined. Calculations were also made for texture characteristics like contrast, correlation, homogeneity, and energy. Additionally, the values for entropy and density were calculated, yielding a total of 33 features for the classifiers to be trained in the MATLAB (Math-Works, MA, USA) environment. To determine the H_2O_2 on PADs, a total of 23 classifiers were trained using all the extracted features.

The performance comparison's classification accuracy was assessed in order to determine which classifier should be included in our Hiperox Sens++ app.

2.1.2.7 Smartphone application: Hi-perox Sens++

To test the proposed colorimetric detection of H_2O_2 , our custom-designed Android application, named Hi-perox Sens++, was developed with improved features in terms of simplicity, speed, test options, and user-friendliness. In comparison to the previous version, which used both the MATLAB and Python environments, the classification process was only run on the remote server under the MATLAB environment in the current version. Additionally, the interface has been enhanced with new screen designs and icons to make it simpler and more intuitive. In Figure 2.3, screenshots of the Hi-perox Sens++ are shown. The main page of the app, as seen in Figure 2.3a, gives users the option to upload an existing photo or take a new one using their smartphone's camera (Figure 2.3b). The image is displayed on the screen once it has been loaded or captured in the application (Figure 2.3c). The ROI is then quantitatively cropped using the crop box as shown in Figure 2.3d. To determine whether the ROI is suitable for analysis, the cropped ROI is displayed (Figure 2.3e). If not, the crop icon can be used to re-crop it. When the upload button is pressed, the ROI is transmitted to the distant server. The remote server's classifier uses the ROI to categorize the concentration value. In order to display the value on the screen, the value is finally sent from the remote server to the Hi-perox Sens++ (Figure 2.3f).

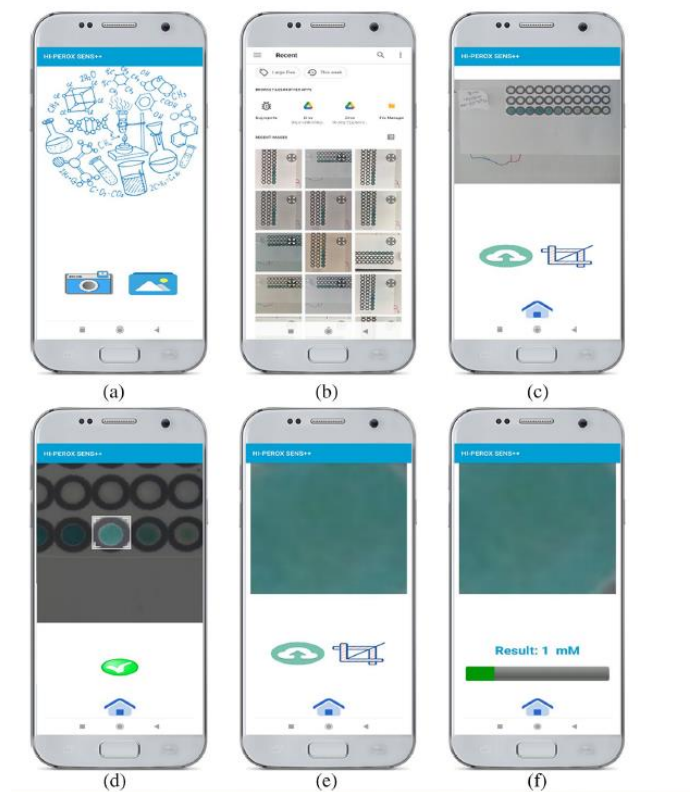


Figure 2.3: Demonstration of colorimetric H₂O₂ quantification procedures on the homepage of the Hi-perox Sens++. The gallery or smartphone camera can be used to select an image as shown in b. The selected image is displayed on the screen in c. The image is cropped using an adjustable crop box, and d displays the cropped area. The cropped patch is uploaded in e for H₂O₂ analysis. Finally, the result is given in f.

2.1.2.8 Selectivity, Stability, and Real Sample Analysis

A selectivity test was conducted using a variety of interferents (CaCl₂, NaCl, KCl, NaHCO₃, MgCl₂, CaCl₂, Na₂SO₄, urea, sucrose, glucose, lactate solutions) at 10 mM to show the specificity of PADs for H₂O₂. The images of μ PADs were taken with a smartphone camera at $t = 30$ s and $t = 10$ min following the addition of each interferent. Following an empirical analysis of the images, the outcomes were contrasted with those obtained using 0 and 5 mM H₂O₂. In addition, a mixture containing all the interfering species was prepared at given concentrations and used for colorimetric testing of 0 and 5 mM H₂O₂. The stability test was conducted with μ PADs stored at 4 °C for 0, 1, 3, 6, and 8 days. Briefly, 5 mM H₂O₂ was added to these μ PADs, and the color change was imaged at 10 min under controlled lighting conditions. Water directly taken from the tap, artificial serum, and FBS were used as real samples to test the classification performance of the system. Only FBS was diluted 50 times with

dH₂O. Varying concentrations of standard H₂O₂ (0, 0.05, 0.1, 0.2, 0.5, 1, and 5 mM) were added to the solutions to prepare the spiked samples.

2.2 Results and Discussion

The XRD patterns of Fe₃O₄ and Fe₃O₄@Chi NPs are displayed in Figure 2.4a. In accordance with the diffraction patterns of the 220°, 311°, 400°, 422°, 511°, and 440° crystal faces of the Fe₃O₄ spinel structure (ICSD #26,410), characteristic peaks were seen at 2θ of 9.6°, 30.1°, 35.5°, 43.1°, 54.5°, 57.6°, and 63.6° (Figure 2.5). Peak broadening suggested that NPs were of a small size. In order to determine the crystallite size of NPs from the XRD data, a modified Debye-Scherrer equation was used. The Fe₃O₄@Chi NPs' broad diffraction peak proves that the amorphous Chi polymer successfully coated the Fe₃O₄ NPs. Additionally, the Fe₃O₄ NP phase did not change as a result of the Chi coating. The Fe₃O₄ spinel type structure is confirmed by the peaks at wavenumbers of 578 and 464 cm⁻¹ in the FTIR spectrum of the material (Figure 2.4b). These peaks are thought to originate from Fe-O bands in tetrahedral and octahedral sites [124,125]. The Fe₃O₄@Chi NPs spectrum, when compared to Fe₃O₄ NPs, showed a number of absorption peaks, indicating the presence of various functional groups in the cross-linked beads. O-H stretching vibrations and amino groups of Chi can be linked to the broadband in the 3000–3600 cm⁻¹ range. At 2931 cm⁻¹, the symmetric and asymmetric aliphatic C-H stretching bands were visible. Chi's C-O stretching vibration of the amide was represented by the bands at 1625 and 1529 cm⁻¹, while the C-O stretching vibration of the C-OH was represented by the band at 1068 cm⁻¹ [126,127]. Additionally, the IR spectrum of Fe₃O₄ @ Chi NPs (580 cm⁻¹) showed the strong characteristic adsorption peaks linked to the Fe-O bond vibration of Fe₃O₄, further supporting the idea that Fe₃O₄ in Fe₃O₄@Chi NPs was formed in situ. [127]. The Chi coating of Fe₃O₄ NP was also confirmed with DLS and TGA (Figure 2.6).

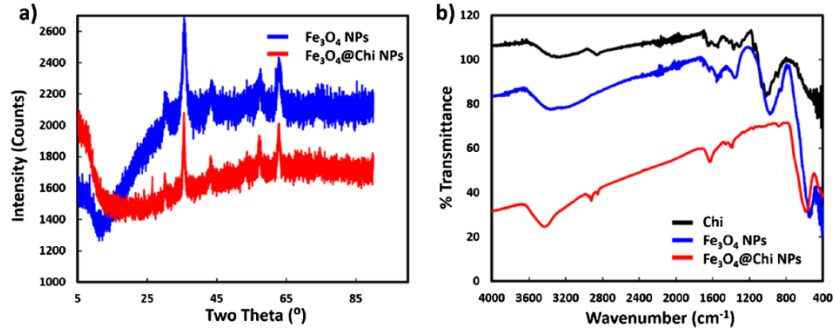


Figure 2.4: XRD (a) and FTIR (b) analysis results of Fe_3O_4 @Chi NPs, Fe_3O_4 and Fe_3O_4 .

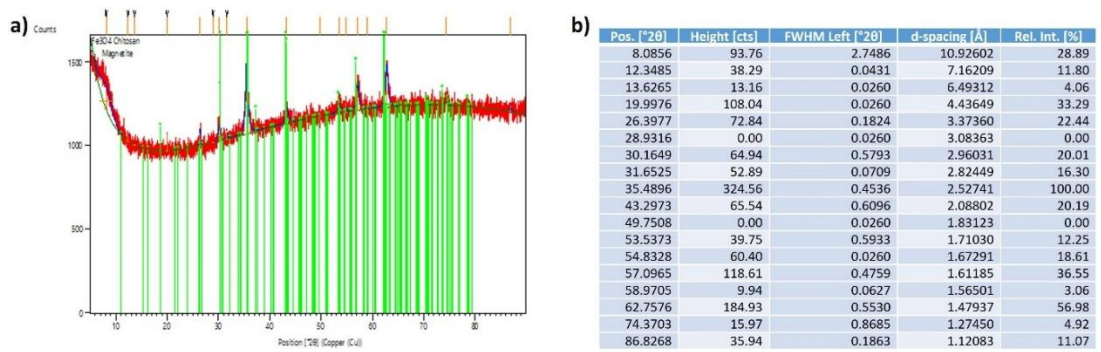


Figure 2.5: Rietveld pattern analysis results and report of Fe_3O_4 @Chi NPs.

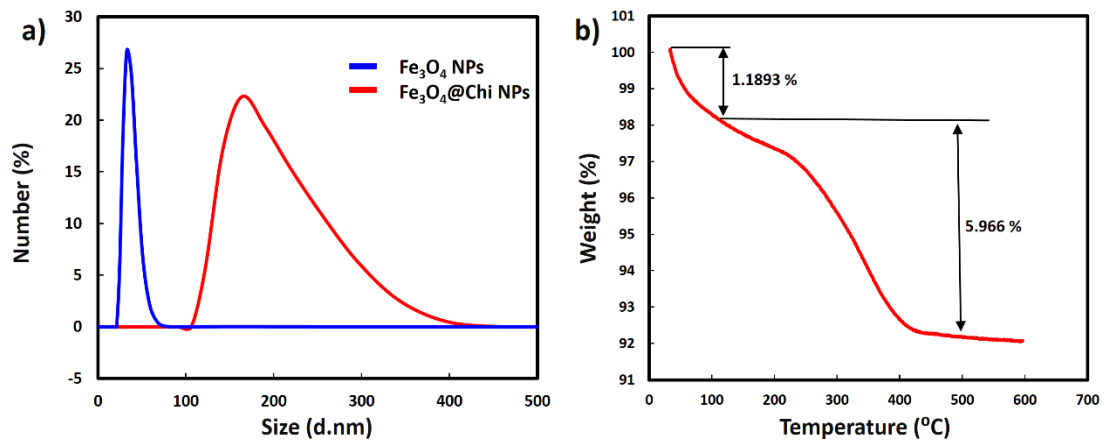


Figure 2.6: DLS (a) and TGA (b) analysis results of Fe_3O_4 @Chi NPs, Fe_3O_4 and Fe_3O_4 .

Using UV-Vis spectroscopy, the efficiency of Fe₃O₄@ Chi NPs for the colorimetric detection of H₂O₂ was evaluated in comparison to TMB, Chi, and Fe₃O₄ NPs. First, the time-dependent UV-Vis absorbance response of Fe₃O₄@ Chi NPs at 645 nm was analyzed. The response reaches a steady state after 100 seconds, as shown in Figure 2.7a, so the response at 120 seconds was used in the subsequent experiments. The chromogenic substance TMB was present in all test groups.

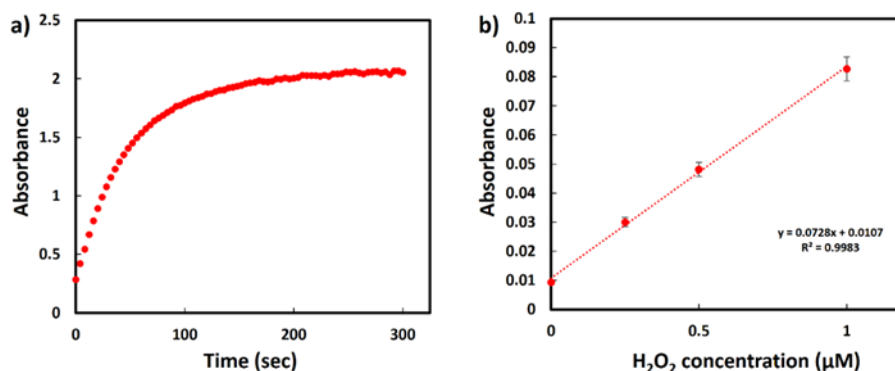


Figure 2.7: Fe₃O₄@Chi NPs' time-dependent reaction to 200 μM of H₂O₂ (a). A calibration curve showing the response of Fe₃O₄@Chi NPs in 0 to 1 μM H₂O₂ (n = 3).

In the cases of only TMB (control) and Fe₃O₄ NPs, as shown in Figures 2.8ai and b-ii, no color change was seen, proving conclusively that these two cannot cause any color change by themselves even in the presence of H₂O₂ at high concentration. As opposed to Chi, which produced a blueish color, H₂O₂ confirmed Chi's catalytic properties for the oxidation of TMB [128,129]. Though it was significantly less than that of Fe₃O₄ @ Chi NPs at 10 μM H₂O₂, the color change was obtained at 200 μM H₂O₂. In other words, Fe₃O₄ @ Chi NPs had significantly better catalytic performance than Chi alone. The detection of H₂O₂ at various concentrations was then performed using Fe₃O₄ @ Chi NPs. Figure 2.8bi unequivocally demonstrates that increasing the H₂O₂ concentration from 1 to 200 μM caused a perceptible color change. Figures 2.8aii and 2.7b show the calibration curve that was created using the UV-Vis absorbance data at 645 nm (Figure 2.8ai).

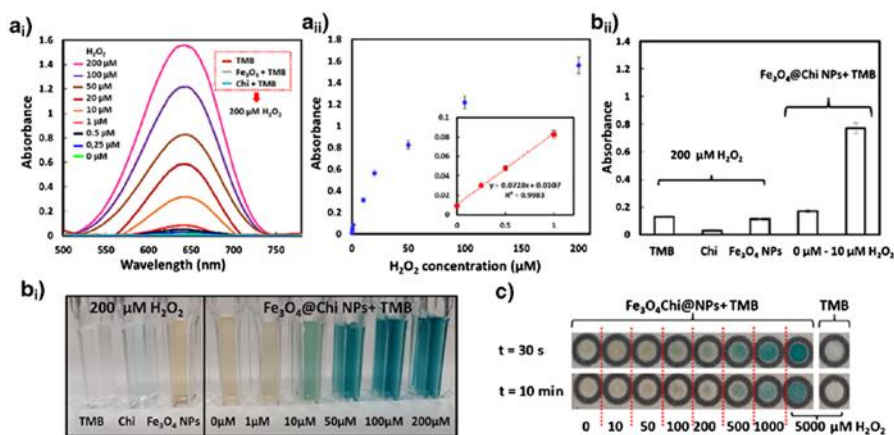


Figure 2.8: UV-Vis spectra of TMB, Fe_3O_4 , and Chi in 200 μM of H_2O_2 (ai), as well as those of Fe_3O_4 @Chi NPs in various concentrations of H_2O_2 . A calibration curve showing the correlation between Fe_3O_4 @Chi NP response and H_2O_2 concentrations ($n = 3$) (aii). The visual color change of TMB, Fe_3O_4 , Chi, and Fe_3O_4 @Chi NPs in solutions of H_2O_2 at various concentrations ($n = 3$), and a comparison of their responses (bii). Fe_3O_4 @Chi NPs' effects on the color of μPADs that can be seen with the naked eye in the presence of TMB and various concentrations of H_2O_2 as opposed to TMB only at 5000 μM of H_2O_2 (c).

The limit of detection (LOD) of the Fe_3O_4 @Chi NPs for the detection of H_2O_2 was calculated to be 69 nM ($\text{LOD} = 3 \times \sigma / \text{Slope}$). Compared to some of the recently published studies, Fe_3O_4 @Chi NPs demonstrated a significantly low LOD with a narrow detection range. Afterward, the Fe_3O_4 @Chi NPs were applied to a μPAD as shown in Figure 2.1 for the colorimetric detection of H_2O_2 using machine learning classifiers, a subset of an artificial approach. First, varying concentration of TMB (20–320 mM) was tested in μPADs to obtain the maximum color intensity. According to the results of 5 mM H_2O_2 ($t = 10$ min), increasing the concentration of TMB had no significant impact in terms of color intensity, and therefore, 20 mM of TMB (0.8 μL) was used in subsequent experiments (Figure 2.9a). As for the nanozyme, it increased the color intensity as well as the background noise as it alone made the detection areas of the μPADs brown (Figure 2.9b). To reduce the background noise and have much uniform color change, 1 μL aliquots of 2 mg mL^{-1} Fe_3O_4 @Chi NPs were used in μPADs . Similarly, increasing the sample volume changes the response as the drying time changes, and the color information changes during drying. Therefore, 2 μL of sample was used in all control and test groups to prevent any interference caused by drying and to have a uniform response as well as a satisfactory color change. The LOD of the μPAD based on color intensity was calculated as 6.5 μM ($\text{LOD} = 3 \times \sigma / \text{Slope}$),

which was higher than that of the UV–Vis absorbance-based detection due to various reasons, including heterogeneous color distribution and noise from the underlying paper structure. However, it still demonstrates the potential of the system to be trained for lower concentrations of H_2O_2 . When compared to a recently published study, the system had a comparable performance with a larger detection range. Unlike the study, the proposed system uses machine learning classifiers for a robust and adaptive H_2O_2 determination based on image features instead of color intensity data or a calibration curve, eliminating the influence of illumination variation and camera optics. The effect of pH on sensing was also tested in a pH range of 3 to 11. According to the results at 10 min, the sensor performed better at acidic and neutral pH than in basic conditions (Figure 2.10).

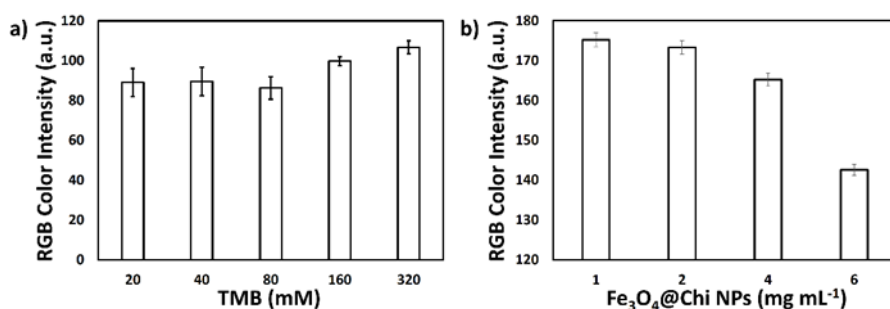


Figure 2.9: The effect of TMB (a) and Fe_3O_4 @Chi (b) NPs on color intensity (t=10 min, n=3).

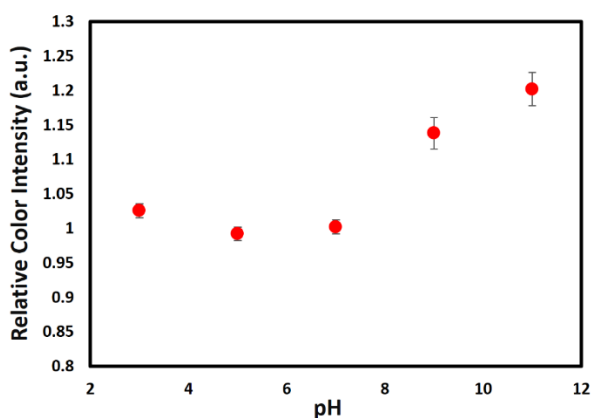


Figure 2.10: The effect of pH at 10 min.

First, images of μPADs detecting H_2O_2 at varying concentrations between 0 and 5 mM at t = 30 s were used to train twenty-three classifiers (Figure 2.8c). 98.7% classification accuracy put linear discriminant analysis (LDA) ahead of the competition in the

performance comparison (Table 2.2). The classification accuracy was then increased to 98.7% for the images taken at $t = 10$ min (Figure 2.8c) using the same techniques. The accuracy shows a small change even after 10 minutes, demonstrating the system's stability. The LDA uses maximum likelihood and Bayesian rules to determine which input and predefined classes have the highest likelihood based on a discriminant function that accurately assigns units to their correct classes with the least amount of error [130]. LDA is used in two steps to obtain the class separation rules. Finding the discriminant functions that will be used to identify the true group of the trained object comes first. Second, based on the assignment rule generated using these functions, it aims to identify the group to which the object will be assigned [131]. The robustness of the system is demonstrated by the confusion matrices shown in Fig. 2.3a-b. Besides classification accuracy (Eq. 1), the performance of the classifiers was also tested for precision (Eq. 2), recall (Eq. 3), and F1-score (Eq. 4).

$$\text{Accuracy} = (\text{TP} + \text{TN}) / (\text{TP} + \text{TN} + \text{FP} + \text{FN}) \quad (1)$$

$$\text{Precision} = \text{TP} / (\text{TP} + \text{FP}) \quad (2)$$

$$\text{Recall} = \text{TP} / (\text{TP} + \text{FN}) \quad (3)$$

$$\text{F1-score} = 2 \times (\text{Precision} \times \text{Recall}) / (\text{Precision} + \text{Recall}) \quad (4)$$

Table 2.2: Classification accuracy results for H_2O_2 with different machine learning classifiers

Machine Learning Classifiers	Classification Accuracy (%)	
	$t = 30$ s	$t = 10$ min
Linear SVM	83.25	74.86
Random Forest	70.81	71.81
Decision Tree	82.80	83.82
Nearest Neighbors (KNN)	63.29	64.63
Bagging Classifier	42.48	44.20
Naive Bayes	68.77	69.03
Gaussian Process	81.04	81.42
Logistic Regression	90.05	90.10
Linear Discriminant Analysis	98.60	98.70
AdaBoost	63.97	64.76
Bernoulli Naive Bayes	84.34	85.38
Extra Tree Classifier	82.46	83.44

Gradient Boosting Classifier	85.74	86.72
RBF SVM	73.83	75.44
Nu SVM	75.28	76.65
Passive Aggressive Classifier	74.64	75.09
QDA	70.40	71.69
Weighted KNN	87.56	88.74
Ensemble Boosted Tree	77.98	78.82
Ensemble Bagged Tree	75.93	76.91
Ensemble Subspace Discriminant	82.02	83.78
Coarse Tree	73.69	72.63
Ensemble RUS Boosted Tree	70.02	71.11

False positives (FPs) are positive predictions that the classifier incorrectly identifies as negative. The positive predictions that the classifier makes are known as TPs (true positives). The number of predictions that are classified as negative is called TN (true negative), and the number of false negatives is known as FN (false negatives) [132]. The accuracy rate of the model, which is the ratio of TP + TN to TP + TN + FP + FN, is the most widely used and straightforward metric to assess performance. The precision is calculated as the product of the TP and the total number of samples predicted to be class positive (TP + FP). The proportion of TP to TP + FN is the recall. Utilizing metrics for precision and recall, the F1-score is determined. Measures of recall and precision by themselves are insufficient to derive a meaningful comparison conclusion. More accurate results are obtained when combining the two evaluation criteria, and the F1 score is calculated as the harmonic mean of precision and recall. [133]. According to the results of the performance metrics (Figure 2.11), LDA had the best accuracy in terms of precision, recall, and F1-score. For $t = 10$ min, classification reports and a confusion matrix are presented in Table 2.3 and Figure 2.12, respectively. The performance metrics' results are below average at concentrations of 0.5 and 5 mM H_2O_2 , which is also evident in the confusion matrix (Figure 2.13), which depicts the performance metrics. In a nutshell, two out of 28 tested samples at 5 mM and one out of 28 tested samples at 0.5 mM were misclassified as 0.2 mM and 0.5 mM, respectively (Figure 2.13a). The confusion matrix's diagonal location of the other concentration results indicates that they were correctly classified. The correlation between the classifier's true and predicted classes can be seen in the confusion matrices. The true and predicted classes of LDA for each value of the H_2O_2 concentration are displayed

in Figure 2.13a-b along with confusion matrices for $t = 30$ s and $t = 10$ min, respectively. The current system showed greater accuracy when compared to the nonenzymatic platform [120]. The current system, in contrast to the platform, can be used to detect some biologically important molecules, including lactate and glucose.

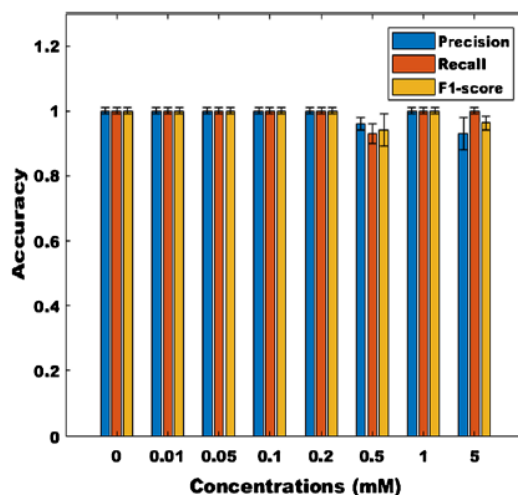


Figure 2.11: The performance of LDA based on precision, recall, and F1-score at $t = 30$ s.

Table 2.3: Evaluation of the LDA for $\text{Fe}_3\text{O}_4@Chi$ at $t=10$ min in terms of precision, recall, and F1-score

	Precision	Recall	F1-score
0 mM	1.00	0.93	0.97
0.01 mM	0.96	1.00	0.98
0.05 mM	0.96	1.00	0.98
0.1 mM	1.00	1.00	1.00
0.2 mM	1.00	1.00	1.00
0.5 mM	1.00	0.97	0.98
1 mM	1.00	1.00	1.00
5 mM	0.96	1.00	0.98
Average	0.99	0.99	0.99

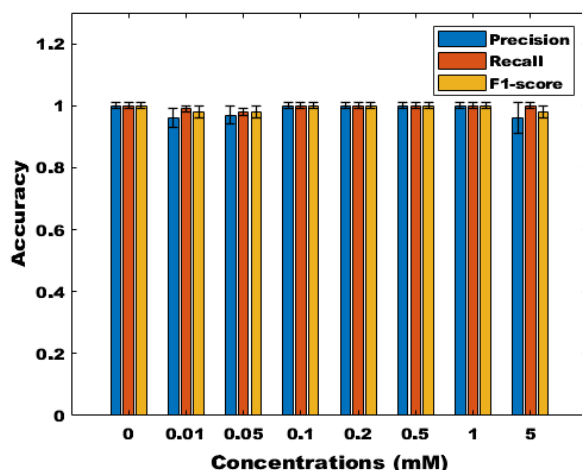


Figure 2.12: Evaluation of LDA with error bars in terms of precision, recall, and F1-score at $t=10$ min for $\text{Fe}_3\text{O}_4@Chi$

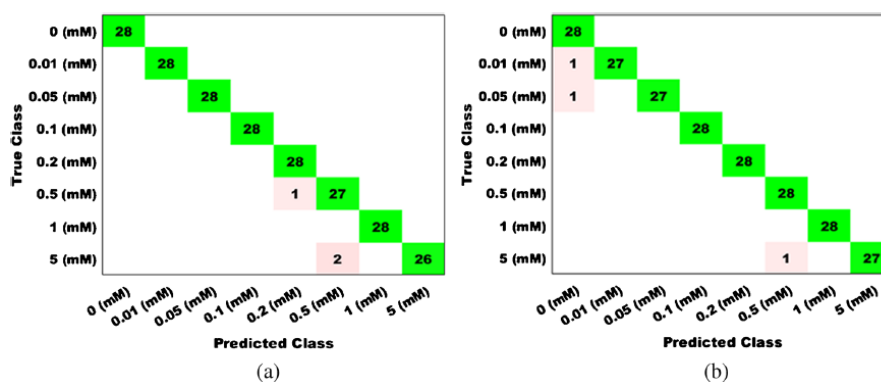


Figure 2.13: Confusion matrices of $\text{Fe}_3\text{O}_4@Chi$ NPs at $t = 30$ s (a) and $t = 10$ min (b) in various H_2O_2 concentrations

Hi-perox Sens++, a user-friendly and easy-to-use smartphone app for H_2O_2 detection, uses the LDA classifier. The app is shown using screenshots in Figure 2.3, where the cropped version of the selected image is sent to a remote server. The result is shown in Hi-perox Sens++ as in Figure 2.3f, where the sample H_2O_2 was correctly identified as 1 mM, following the classification of the concentration level. The proposed system was then tested with tap water, synthetic serum, and FBS to demonstrate its practical applicability. Synthetic serum and FBS resulted in a slightly different color than tap water. Therefore, the machine learning (ML) training dataset was expanded to include these two samples, which demonstrates the adaptability of the system to new conditions. As seen in Table 2.4, an acceptable recovery of H_2O_2 (104.6% for tap

water, 96.9% for synthetic serum and 100.6 for FBS in average, calculated as shown in [134], was achieved with the present system. It is important to note that training the machine learning classifier with additional real samples could increase the system's accuracy even more. A selectivity test was also run using a few interfering species. Real samples contain various chemicals that could potentially interfere with the detection of H_2O_2 [135]. Therefore, various anions and cations present in tap water along with some common organic compounds were tested for the selectivity of the system. The results at 30 s clearly demonstrated that there was no discernible difference between 10 mM interferents and 0 mM H_2O_2 . However, a significant change in color intensity at 5 mM H_2O_2 demonstrated the sensor's H_2O_2 selectivity. All test groups experienced a proportional change in color intensity as the solutions in the μPADs dried after 10 minutes. When a mixture made up of all interfering species was used as a base solution, a comparable reaction was also noticed. In addition, μPADs demonstrated a relatively stable response for 8 days when they were stored in fridge (Figure 2.14). It is worth noting that the μPADs were stored at + 4°C, as TMB causes loss of sensitivity when stored at room temperature. Although machine learning was successfully integrated to the system, it requires internet access for operation. Unlike machine learning, deep learning can be embedded into a smartphone app for off-line analysis. It also automatically extracts features for training. Therefore, deep learning will be integrated to the system in the future. Although the system is robust against illumination variation and camera optics, its robustness can be further improved by including more illumination conditions and smartphones of different brands to the training dataset. In addition, although nanozymes have the potential to overcome some of the disadvantages of natural enzymes in general, they have disadvantages such as low substrate specificity, poor biocompatibility, and potential nanotoxicity [136]. Their catalytic activity also depends on size, shape, structure, and composition. Therefore, it is possible to further improve the catalytic performance of the $\text{Fe}_3\text{O}_4@\text{Chi}$ nanozyme by changing the synthesis conditions.

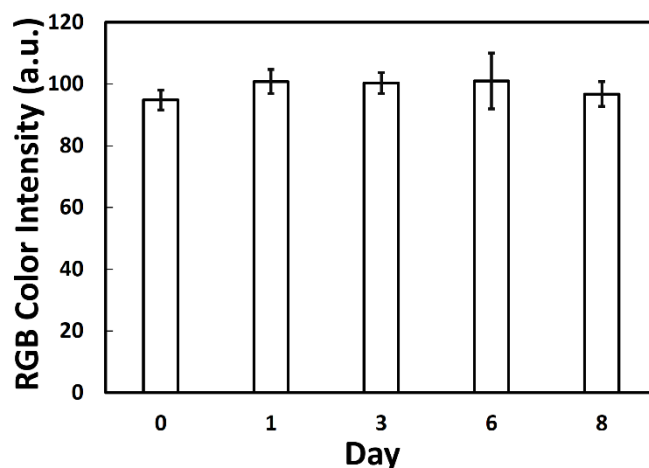


Figure 2.14: Stability of the system for 8 days (n=3).

Table 2.4: Determination of H₂O₂ in tap water, synthetic serum and FBS based on the average of classification results.

Added (mM)	Tap water		Synthetic serum		FBS	
	Found (mM)*	Recovery (%)	Found (mM)*	Recovery (%)	Found (mM)*	Recovery (%)
0	0.014	-	0.007	-	0.00	-
0.05	0.057	114	0.05	100	0.05	100
0.1	0.114	114	0.10	100	0.11	114.3
0.2	0.2	100	0.19	92.9	0.18	89.3
0.5	0.5	100	0.57	114.3	0.50	100
1	1	100	0.86	85.7	1.00	100
5	5	100	4.43	88.6	5.00	100
Average		104.7		96.9		100.6

* The average of classification results

2.3 Conclusion

In this study, a machine learning-based smartphone app was used to determine H_2O_2 using a peroxidase mimicking $\text{Fe}_3\text{O}_4@ \text{Chi}$ nanozyme that was synthesized. The nanozyme displayed excellent peroxidase-like activity and high selectivity in comparison to the control group (only TMB), Fe_3O_4 NPs, and Chi. Although there are numerous studies using nanozymes for UV-Vis-based colorimetric analysis, very few report the use of nanozymes in μPADs , and none use artificial intelligence. To remove the obstacle preventing the widespread use of these excellent materials, particularly in resource-constrained environments, nanozymes must be applied to μPADs . To our knowledge, this is the first study to describe the development of a machine learning-based smartphone app with an intuitive user interface for quick and accurate H_2O_2 analysis in a paper sensor based on nanozymes. High accuracy, repeatability, and robustness against variations in lighting and camera optics were all provided by machine learning. The system can be trained for lower H_2O_2 concentrations, which could increase the system's practical applications due to the sensor's low LOD. Real samples were used to show the system's practical applicability. The tested H_2O_2 concentration range could be useful for processes like wastewater treatment and H_2O_2 testing in the food industry [137]. In conclusion, combining artificial intelligence with a smartphone app makes the analysis portable, simple to use, affordable, adaptable, and robust, all of which may help non-expert users use such analytical tools more effectively.

Chapter 3

3 Smartphone Embedded Deep Learning Approach for Highly Accurate and Automated Colorimetric Lactate Analysis in Sweat

3.1 Materials and Methods

3.1.1 Materials

NaCl ($\geq 99\%$) (Sigma Aldrich, USA), NH_4Cl ($\geq 99\%$) (Sigma Aldrich, USA), urea ($\geq 99\%$) (Sigma Aldrich, USA), lactic acid ($\geq 85\%$) (Sigma Aldrich, USA), acetic acid ($\geq 99\%$) (Sigma Aldrich, USA), NaOH ($\geq 98\%$) (Sigma Aldrich, USA), TMB (Sigma Aldrich, USA), LOx from *Aerococcus viridans* (500 units/mg) (Sigma Aldrich, USA), HRP (≥ 250 units/ mg) (Sigma Aldrich, USA), KCl ($\geq 99\%$) (Sigma Aldrich, USA), D (+)-glucose ($\geq 99\%$) (Sigma Aldrich, USA), sucrose ($\geq 99.5\%$) (Sigma Aldrich, USA), uric acid (UA) ($\geq 99\%$) (Sigma Aldrich, USA), ascorbic acid (AA) ($\geq 99\%$) (Sigma Aldrich, USA), dopamine (DA) ($\geq 97\%$) (Sigma Aldrich, USA), CaCl_2 ($\geq 97\%$) (Sigma Aldrich, USA), Whatman qualitative filter paper - grade 1 (Sigma Aldrich, USA), plaster (Pharmacy, Turkey).

Artificial sweat was prepared according to a previous report [138]; only the lactate concentration was varied for testing as mentioned in the next section.

3.1.2 Methods

3.1.2.1 Design and Fabrication of μ PAD and Patch

The μ PAD was designed using Microsoft PowerPoint 2013 to be printed on Whatman qualitative filter paper. μ PADs were printed using wax printing. Briefly, designed μ PAD pattern transferred onto filter paper using the wax printer (Xerox ColorQube 8900, Xerox Corporation, USA). The designed μ PAD provides the movement of artificial sweat with the help of hydrophilic channels, enabling it to reach the detection area. After printing, the designed μ PAD was placed onto the hot plate to the paper, and penetration of the melted solid ink was placed into the pores of the chromatography paper. The hot plate was set at 180 °C for 120 sec where the wax melted and diffused into the pores of the filter paper, forming hydrophobic channels that allowed controlled fluid flow.

Turning the μ PAD into a lactate patch, a sticking plaster purchased from a local pharmacy. The sticking plaster was cut with a CNC laser cutting machine (Genmitsu 3018-PRO CNC, SainSmart, China) and adjusted only the detection area of the μ PAD was visible. The lactate detecting μ PAD was sandwiched between the plaster and a transparent tape to avoid direct contact between the detection area and the skin.

3.1.2.2 Preparation of Artificial Sweat

Artificial sweat was prepared according to the previous report [138]. Artificial sweat solution is prepared by dissolving 20 g/L NaCl, 17.5 g/L NH₄Cl, 5 g/L CH₄N₂O, 2.5 ml/L C₂H₄O₂, 15 ml/L C₃H₆O₃ in deionized water. The lactic acid concentration was adjusted in artificial sweat solutions according to the value to be measured. The ideal pH environment for the operation of the HRP and LOx enzymes was investigated. The HRP enzyme is active between pH 4.0 and 8.0, and its most stable pH is 5.5 [139]. The LOx enzyme is active between pH 5.7 and 9.5, and its most stable pH is 7.7 [140]. Considering these values, the pH setting of artificial sweat containing 100 mM lactic

acid was measured between 6 and 7 using a pH meter. The lactic acid concentration was then adjusted to 0, 1, 5, 10, 20, and 50 mM concentrations.

3.1.2.3 Colorimetric Detections

The detection areas of the μ PADs were modified by first adding 0.8 μ L TMB and then an enzyme mixture containing 0.2 μ L LOx and 0.8 μ L HRP. After each solution addition, the μ PADs were left to dry for about 10 min at + 4 °C. The colorimetric behavior of μ PADs was evaluated using artificial sweat (Figure 3.1).

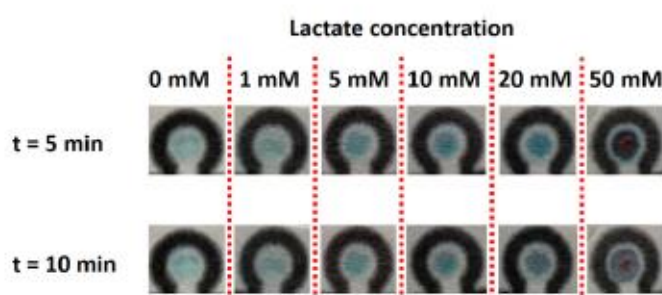


Figure 3.1: Images of μ PADs showing visually observable color changes with varying concentrations of lactate in artificial sweat at $t = 0$ min and $t = 5$ min.

Briefly, μ PADs were immersed in artificial sweat solutions containing lactate at different concentrations (0, 1, 5, 10, 20, and 50 mM), allowing these solutions to reach the detection areas under lateral flow. Color changes in the detection areas were imaged at time points of 0, 5, 10, and 15 min. To turn the μ PAD into a lactate patch, a sticking plaster purchased from a local pharmacy was used. The plaster was cut with a CNC laser cutting machine (Genmitsu 3018-PRO CNC, SainSmart, China) so that only the detection area of the μ PAD was visible. The lactate detecting μ PAD was sandwiched between the plaster and a transparent tape to avoid direct contact between the detection area and the skin. Figure 3.2 shows that schematic illustration of the working principle of systems.

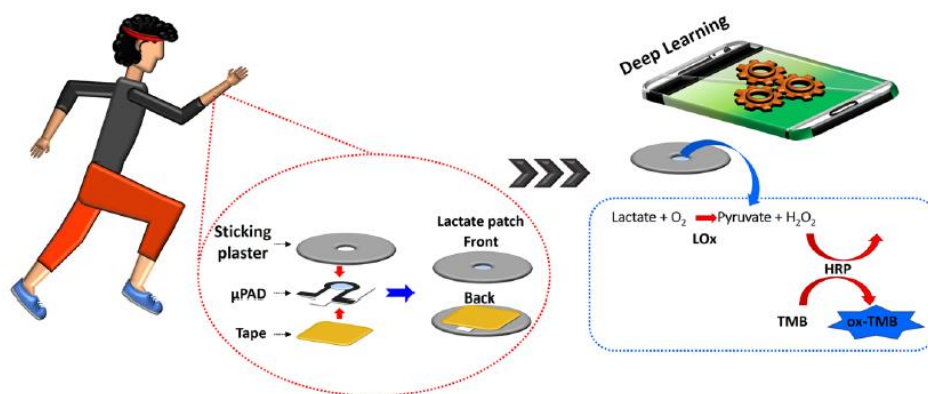


Figure 3.2: A schematic illustration showing the working principle of the system. Lactate is first converted to pyruvate by LOx, releasing H₂O₂ which is then used by HRP for the oxidation of TMB. The color change is imaged using a smartphone camera and the lactate level is determined by DeepLactate, an app running deep learning classifier.

3.1.2.4 Deep Learning

Deep learning is the branch of ML based on neural network architectures, including CNNs [141], recurrent neural networks (RNN) [142], autoencoders [143], transformers [144], and deep belief nets [133]. Among these architectures, CNNs show outstanding performance in processing grid-like topology data such as a digital image (DI). DI represents the visual data in the form of two-dimensional matrix, driven by applications such as classification [145,146], clustering [147], and object recognition [148]. Considering their multi-layered structure, CNNs are very powerful and computationally efficient in image classification as they employ convolution and pooling operations, and perform parameter sharing. Therefore, in this study, several CNN-based deep learning models were tested for quantitative and qualitative analysis of lactate on µPAD images captured with cameras of different smartphones. CNN models mostly follow similar architecture, consisting of convolution and pooling operations, followed by several fully connected layers as demonstrated in Figure 3.3. The convolutional layer is the main block of CNN which applies a convolution filter on the input data to generate a feature map. The output of the convolution layer then passes through pooling operations to reduce the dimensionality, leading to less number of parameters and shortened training time. The convolution and pooling operations may be repeated several times depending on the structure of the architecture. Before the fully connected layer, the output of the final pooling layer is converted to a vector

by flattening. It is the last and most crucial layer of CNN which takes the data from the flatten layer and performs the learning process through the neural network. Here, six CNN models were trained, and it was observed that Inception-v3 outperforms the others in terms of validation and test accuracy. The dataset used in the training of CNN models has a key role in performance as described in the next section.

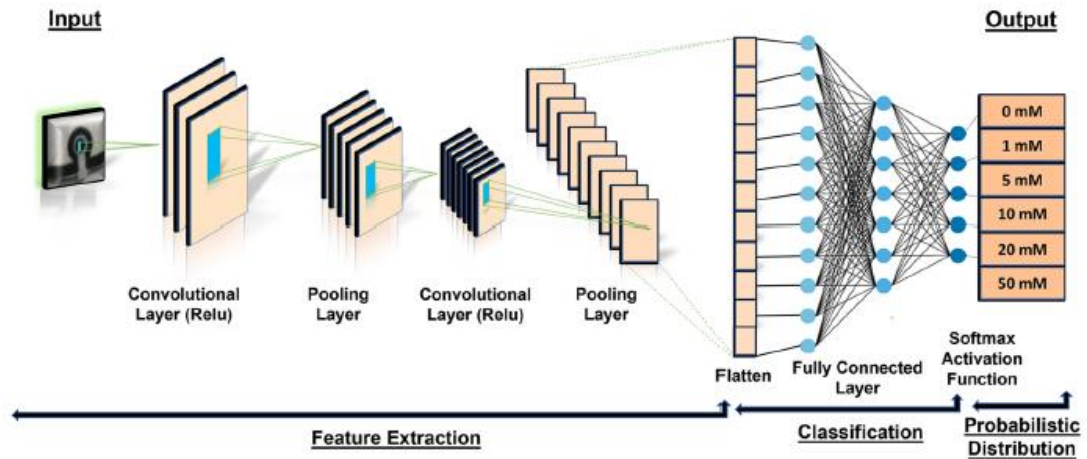


Figure 3.3: General structure of the CNN

3.1.2.5 Image Acquisition

In order for the deep learning models to interpret a given image data accurately under various conditions, the training dataset needs to be fed into the models first, and then validation and testing datasets are used to optimize the parameters of these models. The dataset used for training, validation and testing should contain a sufficient quantity of highquality image captured under various conditions such as rotation, illumination conditions and camera optics. Therefore, image acquisition is a crucial step as it increases the adequacy of the dataset and leads to better performance for deep learning models.

As a proof of concept, the images here were captured under different combinations of three light sources, four smartphone camera optics and five shooting angles to mimic as many varying conditions as possible. In this context, halogen (H), fluorescent (F) and sunlight (S) bulbs were used as light sources. The color temperatures of halogen (Osram 60 W), fluorescent (Klite 6 W) and sunlight (Philips 5.5 W) bulbs are 2700 K (warm), 4000 K (neutral) and 6500 K (cold), respectively. Seven lighting conditions (H, F, S, HF, HS, FS, HFS) were created by switching on these light sources in

different sequences. In addition, images were captured at five different angles (30° , 60° , 90° , 120° , and 150°) with respect to the vertical axis between the μ PAD and smartphone camera. The bulb sources were placed 40 cm away from the smartphones and the distance between each lamp source was 9 cm. The images were captured at an incidence angle of 35° between the sources and μ PAD. Android smartphones of four different brands (Huawei Mate 20 lite, Lenovo P2a42, Oppo A5 2020, and Xiaomi Note 8 Pro) with unique camera properties (Table 3.1) were used for image capturing to ensure interoperability and compatibility. A total of 840 images were captured using the camera settings of the smartphones in automatic mode.

Table 3.1: Camera properties of the smartphones used for imaging.

Smartphone Brand	Image Resolution	Optics	Camera Resolution
Huawei Mate 20 Lite	4000×3000	f/1.8	12 MP
Lenovo P2a42	4032×3024	f/2.2	12 MP
Oppo A5 2020	4000×3000	f/1.8	12 MP
XiaomiNote8Pro	4160×3120	f/2	13 MP

Since the number of images in the dataset affects the performance in deep learning, the number of images was increased with additional methods such as data augmentation. The benefits of data augmentation are two-fold. First, it helps prevent overfitting, which causes the training data to be memorized, making it unable to interpret new data. Second, new images are created based on altering the existing ones, which offers an artificially expanded dataset. Seven methods were employed for augmentation, including a rotation at 90° angles on the horizontal, vertical, and horizontal-vertical axes and square cropping with 180, 240, 300, and 400 pixels. As a result, the total number of images in the dataset reached 10,080. The images were then resized to 400×400 so that the size of the images in the dataset was the same before being fed into the neural networks.

3.1.2.6 Smartphone app: DeepLactate

A smartphone app has been developed for highly sensitive colorimetric lactate analysis in sweat with a deep learning approach. To embed the trained CNN model into Android smartphones, the Tensorflow-Lite (.tflite) library is used to make the model compatible with smartphones. Here, the Inception-v3 model was saved as a data file in the Hierarchical Data Format (HDF - .h5 file) due to its superior performance among the tested CNN models. Then, the “.h5” file was converted to the “.tflite” file using Python, and embedded in our customdesigned DeepLactate app.

DeepLactate having a simple and user-friendly interface is demonstrated in figure 3.4. The home page is given in figure 3.4.a., where an image can be selected from the gallery of the smartphone (figure 3.4b.) or a new image can be captured using the smartphone camera. Then, after selecting or capturing the image from the gallery or camera, the crop alert dialog is displayed to the user (figure 3.4c.). If the user taps the “NO” action, the result is calculated directly (without cropping), as shown in figure 3.4d. Otherwise, the user is directed to the crop screen when the “YES” action is tapped. Next, the region of interest (ROI) on the image is cropped using an adjustable crop box (figure 3.4e) and displayed on the app as shown in figure 3.4f and h. Lastly, the cropped image is loaded to the model using the “UPLOAD” icon to perform the colorimetric lactate analysis and the results are displayed (figure 3.4g. and i) on the app screen.

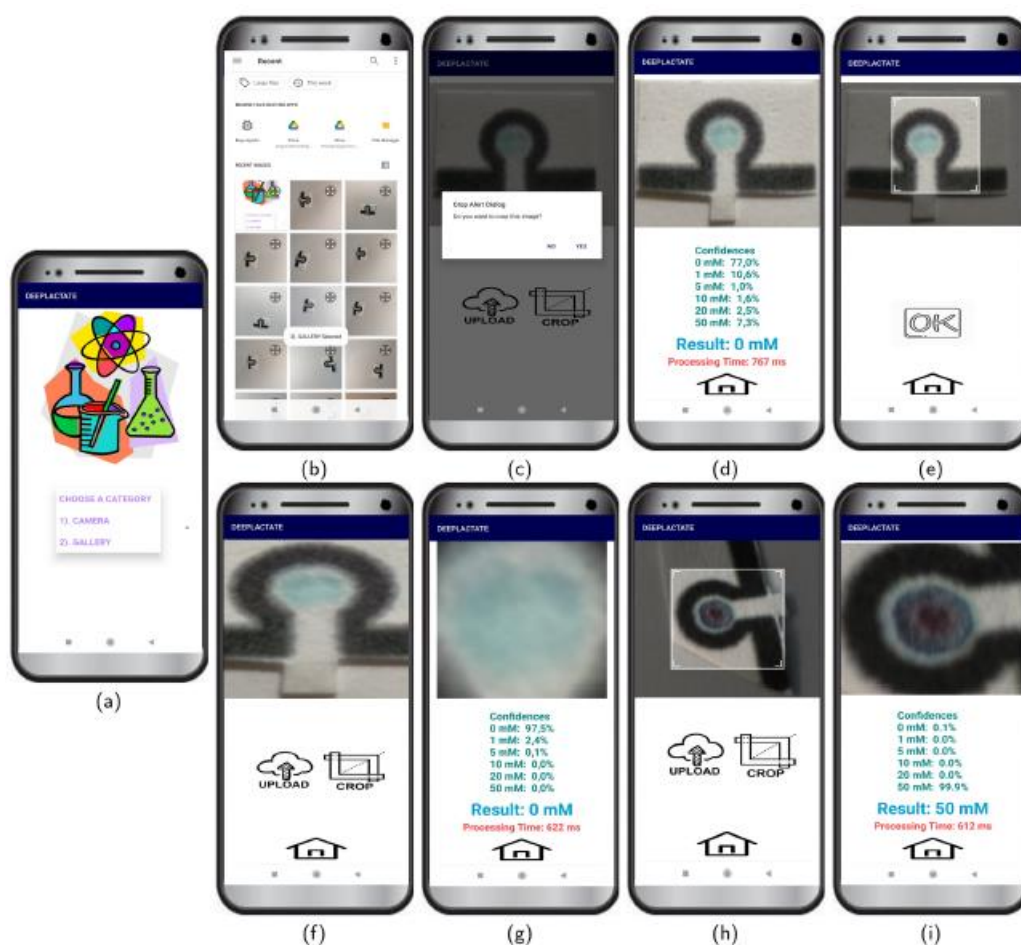


Figure 3.4: The steps for colorimetric lactate analysis in DeepLactate are as follows. The home page of DeepLactate is given in (a). The user can select an image from the gallery in (b) or capture a new image using the smartphone camera. Then, after selecting the image from the gallery, the crop alert dialog is asked to the user as in (c). If the user taps the “NO” action, the result is calculated directly (without cropping) as shown in (d). Otherwise, the user is directed to the crop screen in (e), (f) and (h) when the “YES” action is tapped. The app is tested for the concentrations of 0 mM in (g) and 50 mM in (i).

3.1.2.7 Selectivity, Stability, and Real Sample Analysis

Several potential interfering species were tested for the selectivity of the colorimetric lactate sensor; KCl, glucose, sucrose, AA, UA, DA, and CaCl₂. All species were tested at a concentration of 20 mM, except for uric acid and DA, which were tested at 10 mM. Uric acid and DA were tested at different concentrations because of the dissolving problem, and also their concentration in human sweat. For stability, modified μ PADs were put into +4 °C, and measurements took place at 1, 3, 7, and 14 days. Human sweat analysis took place with the help of two volunteers. Human sweat samples were taken from volunteers resting and jogging (15 min) time (Figure 3.5).

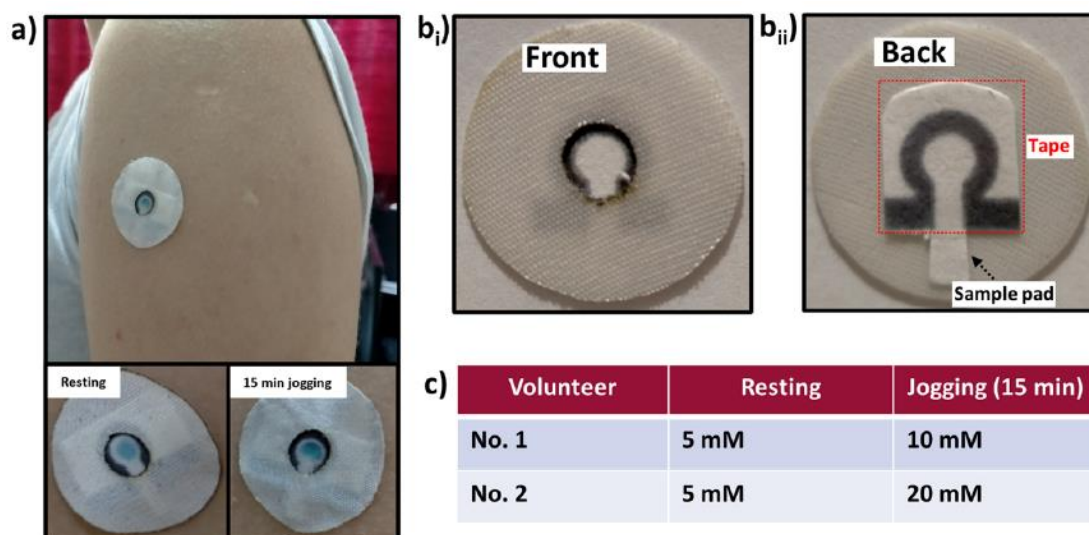


Figure 3.5: An image (a) showing the application of a lactate patch for human sweat analysis. The patch was made by sandwiching a μ PAD between a sticking plaster and a transparent tape (bi-ii). Classification results of the smartphone app DeepLactate for lactate level in the sweat of two volunteers after resting and 15 min jogging.

3.2 Results and Discussion

Here, an offline colorimetric lactate determination method was used with a PAD and a deep learning model integrated into a smartphone app. A sample was intended to be absorbed by the single detection area of the PAD before being transferred to the detection area for colorimetric analysis. For the purpose of determining lactate, the two enzymes LOx and HRP were combined with TMB. Briefly, LOx catalyzes the oxidation of L-lactate to pyruvate and produces H_2O_2 as a by-product [149]. The chromogenic substrate TMB is oxidized by the second enzyme HRP using the byproduct H_2O_2 , resulting in a blueish color change. First, artificial saliva containing varying amounts of lactate was used to test μ PADs.

As seen visually in Figure 3.1, at both the 5 and 10 minute time points, a bluish color formed, and color intensity increased with increasing lactate concentration. Based on the color intensity (RGB data) of images taken by the Oppo A5 2020 at 5 minutes, a detection limit (LOD) of 0.67 mM was calculated ($LOD = 3.3 * \text{/Slope}$). Less than 10 μ l of sample are needed for the μ PAD to finish the analysis. The images of the PADs were taken using four different Android smartphones, each with a different camera configuration (Table 2.1): the Huawei Mate 20 Lite, Lenovo P2a42, Oppo A5 2020, and Xiaomi Note 8 Pro.

For the purpose of training different deep-learning models, a total of 840 images were captured and increased to 10,080 images. Six well-known CNN models were trained in this study using the generated dataset (Section 3.1.2.5). The performance of CNN models is significantly impacted by hyper-parameters like epochs, learning rate, batch size, and optimizer. The epoch was set to 30, the learning rate was set to 0.001, and the batch size was set to 64 under Adam's optimizer, all of which were determined to be suitable based on in-depth experimental studies. When compared to other models, the Inception-v3 model performed the best in terms of validation accuracy, scoring 0.9992 (Table 3.2).

Table 3.2: Experimental results of CNN models.

Models	Validation Accuracy	Test Accuracy
MobileNet	0.9986	0.9869
Xception	0.9990	0.9365
VGG16	0.9926	0.9582
VGG19	0.9965	0.9463
ResNet50	0.9989	0.9767
Inception-v3	0.9992	0.9906

In addition, Figure 3.6 graphically displays the accuracy and loss results for each epoch used in the training and testing of Inception-v3. Besides validation accuracy (Eq. 1), precision (Eq. 2), recall (Eq. 3), F1- score (Eq. 4), and receiver operating characteristic (ROC) curve values were also used in the comparison. While FP (False- Positive) and FN (False-Negative) define the samples that were incorrectly predicted, TP (True-Positive) and TN (True-Negative) describe the number of correctly identified positive and negative samples, respectively. The ratio of correctly predicted samples to all correctly predicted samples is known as precision. The recall is the proportion of actual samples to all of the test set's positive samples. The harmonic mean of the precision and recall values is displayed by the F1-score value.

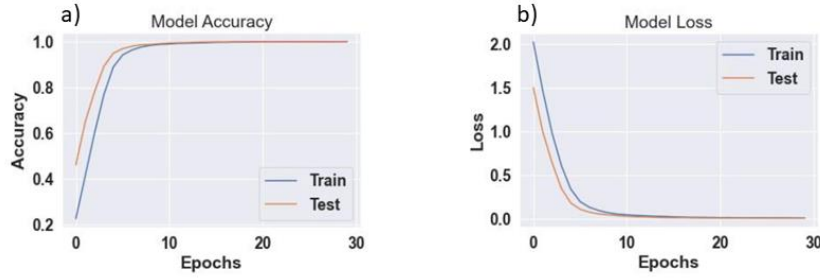


Figure 3.6: Model Accuracy of Inception-v3 is given in (a) and Model Loss of Inception-v3 is shown in (b).

$$\text{Accuracy} = \frac{TP+TN}{TP+TN+FP+FN} \quad (1)$$

$$\text{Precision} = \frac{TP}{TP+FP} \quad (2)$$

$$\text{Recall} = \frac{TP}{TP+FN} \quad (3)$$

$$\text{F1-score} = 2 \times \frac{\text{Precision} \times \text{Recall}}{\text{Precision} + \text{Recall}} \quad (4)$$

The confusion matrix (Figure 3.7) is also used to represent the true and predicted labels, which consist of four indices, including TP, TN, FP, and FN. ROC curves are one of the methods used to measure the success of the models in distinguishing each class. The area under these curves (AUC) approaches show that the CNN model has successfully classified the concentrations. The threshold value was used to classify probability values of colorimetric lactate analysis in artificial sweat and was chosen as 0.5 to obtain the ROC curve. The ROC curve and AUC value of the proposed CNN model (Inception-v3) to detect lactate in artificial sweat were shown in Figure 3.8. The y-axis and x-axis in the ROC curve represent the TP and FP rates, respectively. The Inception-v3 model was tested with 1008 new sample data for each concentration value. In Table 3.3 and Figure 3.7, these performance metrics and the robustness of the system for six different concentration values were illustrated for Inception-v3. Fig. 5 shows that the 5 and 20 mM concentrations deviated from the predicted labels slightly more than the other concentrations. However, the test accuracy was quite close to the validation accuracy and outperformed the other models (Table 3.2). The Inception-v3 model was then included in DeepLactate, a user-friendly and straightforward smartphone app for colorimetric lactate determination in sweat. The

app's screenshots were broken down step by step in Figure 3.4, where the lactate detection of the chosen image from the gallery was shown.

After the concentration classification, the results were displayed in DeepLactate for two different samples, as in Figures 3.4g and i, where the samples were correctly classified as 0 and 50 mM, respectively. In addition, confidence and processing time were given for each concentration value, as shown in Figure 3.4d, to highlight the impact of cropping. The comparison results in Figures 3.4d and 3.4g proved that both confidence (77–97.5 %) and processing times (767 ms - 622 ms) were improved for the same sample as cropping operation reduces the size of the image by removing redundant areas. In addition, the proposed model was robust against rotated images and showed a reliable performance (Figures 3.4h and i). With some interfering species in artificial sweat, the system's selectivity for lactate was tested. By dividing the intensity at $t = 5$ min by the intensity at $t = 0$ min ($I_{t=5}$, $I_{t=0}$), the color intensity for each species was normalized. As shown in Figure 3.9, the color intensity increased only in the case of lactate with time. In other words, only lactate showed higher $I_{t=5}$ than $I_{t=0}$, confirming the selectivity of the system for lactate.

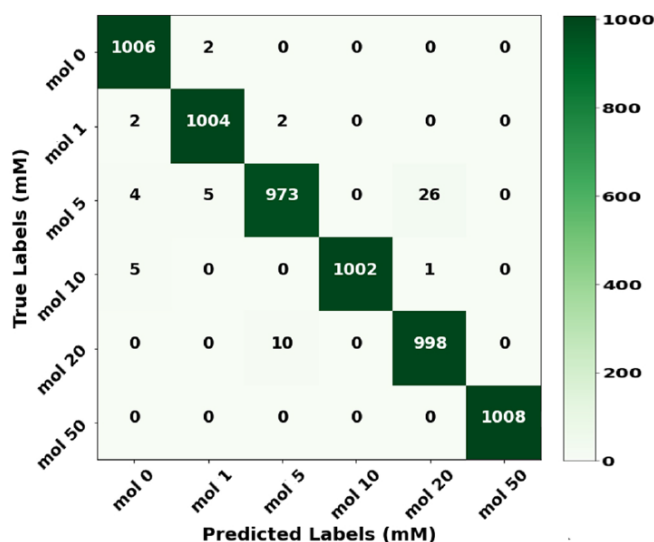


Figure 3.7: Confusion matrix of Inception-v3 in varying concentrations of the test dataset.

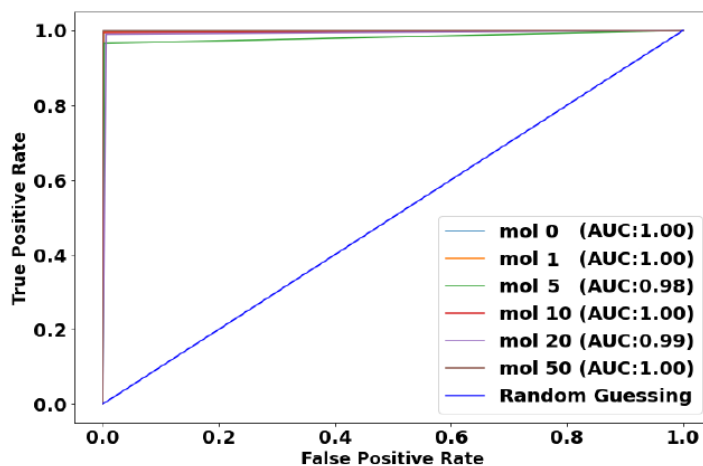


Figure 3.8: ROC curves of Inception-v3 in varying concentrations of the test dataset.

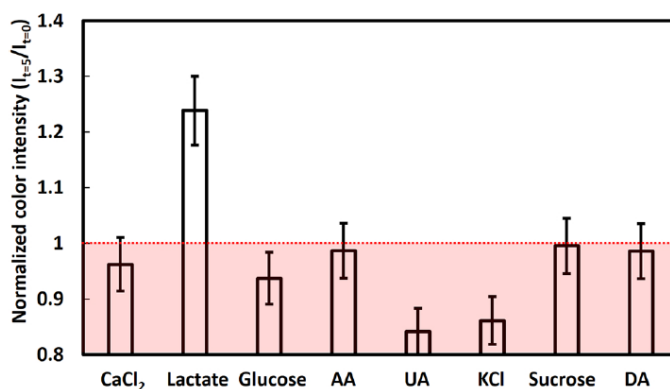


Figure 3.9: Selectivity results based on intensity change (I). The intensity change was normalized by dividing the intensity at $t = 5$ min by the intensity at 0 min ($I_{t=5}/I_{t=0}$).

Lastly, the μ PAD was turned into a patch by sandwiching it between a sticking plaster and a transparent tape as shown in Figures 3.2, 3.5bi, and bii. Briefly, a rectangular tape was used to cover the backside of the μ PAD starting from the hydrophobic boundary (only the Ω shape) in which case a sample pad was left uncovered for sample absorption via capillary force without the use of external equipment (Figures 3.2 and 3.5bii). When using the patch, only the sample pad is in direct contact with the skin, where it absorbs the sweat sample and the channel transfers it to the detection area for detection, avoiding direct contact between the detection area and the skin. This can reduce the potential for skin irritation, a problem frequently observed with current wearable sensors. Since the patch is more like a closed chamber due to its design, the volume of the sample it absorbs is around 8 μ L and doesn't change significantly over the course of analysis. The patch was tested on two volunteers to demonstrate its practical use for human sweat lactate analysis. Sweat lactate was tested for both

volunteers after rest and 15 min of jogging. To stimulate sweat production while resting, the volunteers used plastic wrap. It should be noted that the volunteers produced enough sweat, significantly larger than 8 μL . As can be easily seen in Figures 3.5a and c, the patch successfully detected lactate in human sweat, and the lactate levels in the sweat of both volunteers increased after 15 min of jogging, according to the classification results of DeepLactate. Each patch costs around 40 cents, and unlike commercially available lactate sensors, the system does not require a special reader. Instead, reading is done with a smartphone app that works offline and sweat sample collection is not manual, both of which may significantly contribute to the widespread use of such wearable devices.

3.3 Conclusion

This study describes the classification of lactate in sweat using a deep learning model embedded in a smartphone app called DeepLactate, which also provides the benefit of offline analysis. The deep learning models were trained using images of the μPAD taken in seven illumination conditions using four smartphones of various brands, in order to increase the robustness against illumination variation and ensure inter-phone repeatability. The best-performing model, Inception-v3, was integrated into a smartphone app, enabling quick analysis in a resource-constrained environment because cloud systems are not needed for data sharing with the server. The proposed system can accurately and quickly (within one second) identify lactate in sweat, showcasing its great potential for colorimetric analysis. The system was also put through its paces on volunteers, and the classification outcomes of the app amply illustrated the rise in sweat lactate following jogging. This study is the first that, to the best of our knowledge, links deep learning with both quantitative and qualitative colorimetric analysis of chemical species. It should be noted that training the system with closer concentration levels can also increase the proposed system's classification sensitivity. The proposed system could be easily applied for multi-analyte detection in actual samples like water, urine, and blood as well as for clinical and environmental monitoring in remote and resource-constrained settings.

References

- [1] Cui F, Yue Y, Zhang Y, Zhang Z, Zhou HS. Advancing Biosensors with Machine Learning. *ACS Sens* 2020;5:3346–64. <https://doi.org/10.1021/acssensors.0c01424>.
- [2] Carpenter A, Paulsen I, Williams T. Blueprints for Biosensors: Design, Limitations, and Applications. *Genes* 2018;9:375. <https://doi.org/10.3390/genes9080375>.
- [3] Meshram BD, Agrawal AK, Adil S, Ranvir S, Sande KK. Biosensor and its Application in Food and Dairy Industry: A Review. *Int J Curr Microbiol Appl Sci* 2018;7:3305–24. <https://doi.org/10.20546/ijcmas.2018.702.397>.
- [4] Naresh Varnakavi, Lee N. A Review on Biosensors and Recent Development of Nanostructured Materials-Enabled Biosensors. *Sensors* 2021;21:1109. <https://doi.org/10.3390/s21041109>.
- [5] Damborský P, Švitel J, Katrlík J. Optical biosensors. *Essays Biochem* 2016;60:91–100. <https://doi.org/10.1042/EBC20150010>.
- [6] Chen C, Wang J. Optical biosensors: an exhaustive and comprehensive review. *The Analyst* 2020;145:1605–28. <https://doi.org/10.1039/C9AN01998G>.
- [7] Garzón V, Pinacho D, Bustos R-H, Garzón G, Bustamante S. Optical Biosensors for Therapeutic Drug Monitoring. *Biosensors* 2019;9:132. <https://doi.org/10.3390/bios9040132>.
- [8] Kassal P, Horak E, Sigurnjak M, Steinberg MD, Steinberg IM. Wireless and mobile optical chemical sensors and biosensors. *Rev Anal Chem* 2018;37. <https://doi.org/10.1515/revac-2017-0024>.

- [9] Chen Y, Liu J, Yang Z, Wilkinson JS, Zhou X. Optical biosensors based on refractometric sensing schemes: A review. *Biosens Bioelectron* 2019;144:111693. <https://doi.org/10.1016/j.bios.2019.111693>.
- [10] Long F, Zhu A, Shi H. Recent Advances in Optical Biosensors for Environmental Monitoring and Early Warning. *Sensors* 2013;13:13928–48. <https://doi.org/10.3390/s131013928>.
- [11] Sharma S, Ghosh KS. Overview on recently reported fluorometric sensors for the detection of copper ion based on internal charge transfer (ICT), paramagnetic effect and aggregation induced emission (AIE) mechanisms. *J Mol Struct* 2021;1237:130324. <https://doi.org/10.1016/j.molstruc.2021.130324>.
- [12] Saboorizadeh B, Zare-Dorabei R, Shahbazi N. Green synthesis of carbon quantum dots and their application as a fluorometric sensor for highly selective determination of 6-mercaptopurine in biological samples. *J Taiwan Inst Chem Eng* 2021;129:389–95. <https://doi.org/10.1016/j.jtice.2021.09.015>.
- [13] Pomal NC, Bhatt KD, Modi KM, Desai AL, Patel NP, Kongor A, et al. Functionalized Silver Nanoparticles as Colorimetric and Fluorimetric Sensor for Environmentally Toxic Mercury Ions: An Overview. *J Fluoresc* 2021;31:635–49. <https://doi.org/10.1007/s10895-021-02699-z>.
- [14] Suguna S, David CI, Prabhu J, Nandhakumar R. Functionalized graphene oxide materials for the fluorometric sensing of various analytes: a mini review. *Mater Adv* 2021;2:6197–212. <https://doi.org/10.1039/D1MA00467K>.
- [15] Singh AK, Mittal S, Das M, Saharia A, Tiwari M. Optical biosensors: a decade in review. *Alex Eng J* 2023;67:673–91. <https://doi.org/10.1016/j.aej.2022.12.040>.
- [16] Zhang Z, Liu T, Wang S, Ma J, Zhou T, Wang F, et al. DNA-templated gold nanocluster as a novel fluorometric sensor for glutathione determination. *J Photochem Photobiol Chem* 2019;370:89–93. <https://doi.org/10.1016/j.jphotochem.2018.10.021>.
- [17] Chandra S, Bano D, Sahoo K, Kumar D, Kumar V, Kumar Yadav P, et al. Synthesis of fluorescent carbon quantum dots from *Jatropha* fruits and their application

in fluorometric sensor for the detection of chlorpyrifos. *Microchem J* 2022;172:106953. <https://doi.org/10.1016/j.microc.2021.106953>.

[18] Shumeiko V, Paltiel Y, Bisker G, Hayouka Z, Shoseyov O. A Paper-Based Near-Infrared Optical Biosensor for Quantitative Detection of Protease Activity Using Peptide-Encapsulated SWCNTs. *Sensors* 2020;20:5247. <https://doi.org/10.3390/s20185247>.

[19] Rachim VP, Chung W-Y. Wearable-band type visible-near infrared optical biosensor for non-invasive blood glucose monitoring. *Sens Actuators B Chem* 2019;286:173–80. <https://doi.org/10.1016/j.snb.2019.01.121>.

[20] Ning Y, Zhu M, Zhang J-L. Near-infrared (NIR) lanthanide molecular probes for bioimaging and biosensing. *Coord Chem Rev* 2019;399:213028. <https://doi.org/10.1016/j.ccr.2019.213028>.

[21] Shumeiko V, Paltiel Y, Bisker G, Hayouka Z, Shoseyov O. A nanoscale paper-based near-infrared optical nose (NIRON). *Biosens Bioelectron* 2021;172:112763. <https://doi.org/10.1016/j.bios.2020.112763>.

[22] Patel SK, Parmar J, Kosta YP, Ladumor M, Zakaria R, Nguyen TK, et al. Design of graphene metasurface based sensitive infrared biosensor. *Sens Actuators Phys* 2020;301:111767. <https://doi.org/10.1016/j.sna.2019.111767>.

[23] Li Z, Zhu Y, Hao Y, Gao M, Lu M, Stein A, et al. Hybrid Metasurface-Based Mid-Infrared Biosensor for Simultaneous Quantification and Identification of Monolayer Protein. *ACS Photonics* 2019;6:501–9. <https://doi.org/10.1021/acsp Photonics.8b01470>.

[24] Mehrvar M, Bis C, Scharer JM, Moo-Young M, Luong JH. Fiber-Optic Biosensors—Trends and Advances. *Anal Sci* 2000;16:677–92. <https://doi.org/10.2116/analsci.16.677>.

[25] Marazuela M, Moreno-Bondi M. Fiber-optic biosensors – an overview. *Anal Bioanal Chem* 2002;372:664–82. <https://doi.org/10.1007/s00216-002-1235-9>.

- [26] Leung A, Shankar PM, Mutharasan R. A review of fiber-optic biosensors. *Sens Actuators B Chem* 2007;125:688–703. <https://doi.org/10.1016/j.snb.2007.03.010>.
- [27] Naessens M, Leclerc JC, Tran-Minh C. Fiber Optic Biosensor Using *Chlorella vulgaris* for Determination of Toxic Compounds. *Ecotoxicol Environ Saf* 2000;46:181–5. <https://doi.org/10.1006/eesa.1999.1904>.
- [28] Murugan D, Bhatia H, Sai VVR, Satija J. P-FAB: A Fiber-Optic Biosensor Device for Rapid Detection of COVID-19. *Trans Indian Natl Acad Eng* 2020;5:211–5. <https://doi.org/10.1007/s41403-020-00122-w>.
- [29] Choi C-K, Shaban SM, Moon B-S, Pyun D-G, Kim D-H. Smartphone-assisted point-of-care colorimetric biosensor for the detection of urea via pH-mediated AgNPs growth. *Anal Chim Acta* 2021;1170:338630. <https://doi.org/10.1016/j.aca.2021.338630>.
- [30] Song Y, Wei W, Qu X. Colorimetric Biosensing Using Smart Materials. *Adv Mater* 2011;23:4215–36. <https://doi.org/10.1002/adma.201101853>.
- [31] Zhu W, Li L, Zhou Z, Yang X, Hao N, Guo Y, et al. A colorimetric biosensor for simultaneous ochratoxin A and aflatoxins B1 detection in agricultural products. *Food Chem* 2020;319:126544. <https://doi.org/10.1016/j.foodchem.2020.126544>.
- [32] Yang T, Luo Z, Tian Y, Qian C, Duan Y. Design strategies of AuNPs-based nucleic acid colorimetric biosensors. *TrAC Trends Anal Chem* 2020;124:115795. <https://doi.org/10.1016/j.trac.2019.115795>.
- [33] Zhu D, Liu B, Wei G. Two-Dimensional Material-Based Colorimetric Biosensors: A Review. *Biosensors* 2021;11:259. <https://doi.org/10.3390/bios11080259>.
- [34] Liu P, Yang X, Sun S, Wang Q, Wang K, Huang J, et al. Enzyme-Free Colorimetric Detection of DNA by Using Gold Nanoparticles and Hybridization Chain Reaction Amplification. *Anal Chem* 2013;85:7689–95. <https://doi.org/10.1021/ac4001157>.

- [35] Zheng L, Cai G, Wang S, Liao M, Li Y, Lin J. A microfluidic colorimetric biosensor for rapid detection of Escherichia coli O157:H7 using gold nanoparticle aggregation and smart phone imaging. *Biosens Bioelectron* 2019;124–125:143–9. <https://doi.org/10.1016/j.bios.2018.10.006>.
- [36] Yu T, Xu H, Zhao Y, Han Y, Zhang Y, Zhang J, et al. Aptamer based high throughput colorimetric biosensor for detection of staphylococcus aureus. *Sci Rep* 2020;10:9190. <https://doi.org/10.1038/s41598-020-66105-7>.
- [37] Zeng R, Wang J, Wang Q, Tang D, Lin Y. Horseradish peroxidase-encapsulated DNA nanoflowers: An innovative signal-generation tag for colorimetric biosensor. *Talanta* 2021;221:121600. <https://doi.org/10.1016/j.talanta.2020.121600>.
- [38] Cate DM, Adkins JA, Mettakoonpitak J, Henry CS. Recent Developments in Paper-Based Microfluidic Devices. *Anal Chem* 2015;87:19–41. <https://doi.org/10.1021/ac503968p>.
- [39] Santhiago M, Nery EW, Santos GP, Kubota LT. Microfluidic paper-based devices for bioanalytical applications. *Bioanalysis* 2014;6:89–106. <https://doi.org/10.4155/bio.13.296>.
- [40] Selvakumar B, Kathiravan A. Sensory materials for microfluidic paper based analytical devices - A review. *Talanta* 2021;235:122733. <https://doi.org/10.1016/j.talanta.2021.122733>.
- [41] West PW. Selective Spot Test for Copper. *Ind Eng Chem Anal Ed* 1945;17:740–1. <https://doi.org/10.1021/i560147a024>.
- [42] Comer JP. Semiquantitative Specific Test Paper for Glucose in Urine. *Anal Chem* 1956;28:1748–50. <https://doi.org/10.1021/ac60119a030>.
- [43] Schersten B, Kuhl C, Hollender A, Ekman R. Blood Glucose Measurement with Dextrostix and New Reflectance Meter. *BMJ* 1974;3:384–7. <https://doi.org/10.1136/bmj.3.5927.384>.

- [44] Terry SC, Jerman JH, Angell JB. A gas chromatographic air analyzer fabricated on a silicon wafer. *IEEE Trans Electron Devices* 1979;26:1880–6. <https://doi.org/10.1109/T-ED.1979.19791>.
- [45] Zheng W, Wang K, Xu H, Zheng C, Cao B, Qin Q, et al. Strategies for the detection of target analytes using microfluidic paper-based analytical devices. *Anal Bioanal Chem* 2021;413:2429–45. <https://doi.org/10.1007/s00216-021-03213-x>.
- [46] Martinez AW, Phillips ST, Whitesides GM, Carrilho E. Diagnostics for the Developing World: Microfluidic Paper-Based Analytical Devices. *Anal Chem* 2010;82:3–10. <https://doi.org/10.1021/ac9013989>.
- [47] Morbioli GG, Mazzu-Nascimento T, Stockton AM, Carrilho E. Technical aspects and challenges of colorimetric detection with microfluidic paper-based analytical devices (μ PADs) - A review. *Anal Chim Acta* 2017;970:1–22. <https://doi.org/10.1016/j.aca.2017.03.037>.
- [48] Fu L-M, Wang Y-N. Detection methods and applications of microfluidic paper-based analytical devices. *TrAC Trends Anal Chem* 2018;107:196–211. <https://doi.org/10.1016/j.trac.2018.08.018>.
- [49] Wang K, Yang J, Xu H, Cao B, Qin Q, Liao X, et al. Smartphone-imaged multilayered paper-based analytical device for colorimetric analysis of carcinoembryonic antigen. *Anal Bioanal Chem* 2020;412:2517–28. <https://doi.org/10.1007/s00216-020-02475-1>.
- [50] Peters KL, Corbin I, Kaufman LM, Zreibe K, Blanes L, McCord BR. Simultaneous colorimetric detection of improvised explosive compounds using microfluidic paper-based analytical devices (μ PADs). *Anal Methods* 2015;7:63–70. <https://doi.org/10.1039/C4AY01677G>.
- [51] Ueland M, Blanes L, Taudte RV, Stuart BH, Cole N, Willis P, et al. Capillary-driven microfluidic paper-based analytical devices for lab on a chip screening of explosive residues in soil. *J Chromatogr A* 2016;1436:28–33. <https://doi.org/10.1016/j.chroma.2016.01.054>.

- [52] Martinez AW, Phillips ST, Butte MJ, Whitesides GM. Patterned Paper as a Platform for Inexpensive, Low-Volume, Portable Bioassays. *Angew Chem Int Ed* 2007;46:1318–20. <https://doi.org/10.1002/anie.200603817>.
- [53] Xia Y, Si J, Li Z. Fabrication techniques for microfluidic paper-based analytical devices and their applications for biological testing: A review. *Biosens Bioelectron* 2016;77:774–89. <https://doi.org/10.1016/j.bios.2015.10.032>.
- [54] Strong EB, Schultz SA, Martinez AW, Martinez NW. Fabrication of Miniaturized Paper-Based Microfluidic Devices (MicroPADs). *Sci Rep* 2019;9:7. <https://doi.org/10.1038/s41598-018-37029-0>.
- [55] Ozer T, McMahon C, Henry CS. Advances in Paper-Based Analytical Devices. *Annu Rev Anal Chem* 2020;13:85–109. <https://doi.org/10.1146/annurev-anchem-061318-114845>.
- [56] He Y, Wu Y, Fu J-Z, Wu W-B. Fabrication of paper-based microfluidic analysis devices: a review. *RSC Adv* 2015;5:78109–27. <https://doi.org/10.1039/C5RA09188H>.
- [57] Lim, Jafry, Lee. Fabrication, Flow Control, and Applications of Microfluidic Paper-Based Analytical Devices. *Molecules* 2019;24:2869. <https://doi.org/10.3390/molecules24162869>.
- [58] Singh A, Lantigua D, Meka A, Taing S, Pandher M, Camci-Unal G. Paper-Based Sensors: Emerging Themes and Applications. *Sensors* 2018;18:2838. <https://doi.org/10.3390/s18092838>.
- [59] Lu Y, Shi W, Jiang L, Qin J, Lin B. Rapid prototyping of paper-based microfluidics with wax for low-cost, portable bioassay. *ELECTROPHORESIS* 2009;30:1497–500. <https://doi.org/10.1002/elps.200800563>.
- [60] Olkkonen J, Lehtinen K, Erho T. Flexographically Printed Fluidic Structures in Paper. *Anal Chem* 2010;82:10246–50. <https://doi.org/10.1021/ac1027066>.
- [61] Gölcez T, Kiliç V, Şen M. A Portable Smartphone-based Platform with an Offline Image-processing Tool for the Rapid Paper-based Colorimetric Detection of

Glucose in Artificial Saliva. *Anal Sci* 2021;37:561–7. <https://doi.org/10.2116/analsci.20P262>.

[62] Trofimchuk E, Hu Y, Nilghaz A, Hua MZ, Sun S, Lu X. Development of paper-based microfluidic device for the determination of nitrite in meat. *Food Chem* 2020;316:126396. <https://doi.org/10.1016/j.foodchem.2020.126396>.

[63] Mercan ÖB, Kılıç V, Şen M. Machine learning-based colorimetric determination of glucose in artificial saliva with different reagents using a smartphone coupled μ PAD. *Sens Actuators B Chem* 2021;329:129037. <https://doi.org/10.1016/j.snb.2020.129037>.

[64] Zheng W, Wang K, Xu H, Zhu A, Li T, Cheng Y, et al. Rapid Detection and Quantification of Paper-Based Microfluidics Using Machine Learning. *SSRN Electron J* 2021. <https://doi.org/10.2139/ssrn.3989551>.

[65] Sousa LR, Silva-Neto HA, Castro LF, Oliveira KA, Figueredo F, Cortón E, et al. “Do it yourself” protocol to fabricate dual-detection paper-based analytical device for salivary biomarker analysis. *Anal Bioanal Chem* 2023. <https://doi.org/10.1007/s00216-023-04581-2>.

[66] Yu L, Hao L, Meiqiong T, Jiaoqi H, Wei L, Jinying D, et al. The medical application of terahertz technology in non-invasive detection of cells and tissues: opportunities and challenges. *RSC Adv* 2019;9:9354–63. <https://doi.org/10.1039/C8RA10605C>.

[67] Azmi NE, Rashid AHAb, Abdullah J, Yusof NA, Sidek H. Fluorescence biosensor based on encapsulated quantum dots/enzymes/sol-gel for non-invasive detection of uric acid. *J Lumin* 2018;202:309–15. <https://doi.org/10.1016/j.jlumin.2018.05.075>.

[68] Derbyshire PJ, Barr H, Davis F, Higson SPJ. Lactate in human sweat: a critical review of research to the present day. *J Physiol Sci* 2012;62:429–40. <https://doi.org/10.1007/s12576-012-0213-z>.

- [69] Coyle S, Curto VF, Benito-Lopez F, Florea L, Diamond D. Wearable Bio and Chemical Sensors. *Wearable Sens.*, Elsevier; 2014, p. 65–83. <https://doi.org/10.1016/B978-0-12-418662-0.00002-7>.
- [70] Sapse AT. Proteins in Human Tears: I. Immunoelectrophoretic Patterns. *Arch Ophthalmol* 1969;81:815. <https://doi.org/10.1001/archopht.1969.00990010817012>.
- [71] Bishop DK, La Belle JT, Vossler SR, Patel DR, Cook CB. A Disposable Tear Glucose Biosensor--Part 1: Design and Concept Testing. *J Diabetes Sci Technol* 2010;4:299–306. <https://doi.org/10.1177/193229681000400209>.
- [72] Seal DV, Mackie IA, Coakes RL, Farooqi B. Quantitative tear lysozyme assay: a new technique for transporting specimens. *Br J Ophthalmol* 1980;64:700–4. <https://doi.org/10.1136/bjo.64.9.700>.
- [73] Paterson CA, O'Rourke MC. Vitamin C Levels in Human Tears. *Arch Ophthalmol* 1987;105:376–7. <https://doi.org/10.1001/archopht.1987.01060030096034>.
- [74] Chen Y-L, Kuan W-H, Liu C-L. Comparative Study of the Composition of Sweat from Eccrine and Apocrine Sweat Glands during Exercise and in Heat. *Int J Environ Res Public Health* 2020;17:3377. <https://doi.org/10.3390/ijerph17103377>.
- [75] Chicharro JL, Lucía A, Pérez M, Vaquero AF, Ureña R. Saliva Composition and Exercise. *Sports Med* 1998;26:17–27. <https://doi.org/10.2165/00007256-199826010-00002>.
- [76] Papacosta E, Nassis GP. Saliva as a tool for monitoring steroid, peptide and immune markers in sport and exercise science. *J Sci Med Sport* 2011;14:424–34. <https://doi.org/10.1016/j.jsams.2011.03.004>.
- [77] Sarigul N, Korkmaz F, Kurultak İ. A New Artificial Urine Protocol to Better Imitate Human Urine. *Sci Rep* 2019;9:20159. <https://doi.org/10.1038/s41598-019-56693-4>.
- [78] Xiao G, He J, Qiao Y, Wang F, Xia Q, Wang X, et al. Facile and Low-Cost Fabrication of a Thread/Paper-Based Wearable System for Simultaneous Detection of

Lactate and pH in Human Sweat. *Adv Fiber Mater* 2020;2:265–78. <https://doi.org/10.1007/s42765-020-00046-8>.

[79] Bordbar MM, Samadinia H, Sheini A, Aboonajmi J, Javid M, Sharghi H, et al. Non-invasive detection of COVID-19 using a microfluidic-based colorimetric sensor array sensitive to urinary metabolites. *Microchim Acta* 2022;189:316. <https://doi.org/10.1007/s00604-022-05423-1>.

[80] Hage R, Lienke A. Applications of Transition-Metal Catalysts to Textile and Wood-Pulp Bleaching. *Angew Chem Int Ed* 2006;45:206–22. <https://doi.org/10.1002/anie.200500525>.

[81] Campos-Martin JM, Blanco-Brieva G, Fierro JLG. Hydrogen Peroxide Synthesis: An Outlook beyond the Anthraquinone Process. *Angew Chem Int Ed* 2006;45:6962–84. <https://doi.org/10.1002/anie.200503779>.

[82] Falagas ME, Thomaidis PC, Kotsantis IK, Sgouros K, Samonis G, Karageorgopoulos DE. Airborne hydrogen peroxide for disinfection of the hospital environment and infection control: a systematic review. *J Hosp Infect* 2011;78:171–7. <https://doi.org/10.1016/j.jhin.2010.12.006>.

[83] Sies H. Hydrogen peroxide as a central redox signaling molecule in physiological oxidative stress: Oxidative eustress. *Redox Biol* 2017;11:613–9. <https://doi.org/10.1016/j.redox.2016.12.035>.

[84] Patella B, Inguanta R, Piazza S, Sunseri C. A nanostructured sensor of hydrogen peroxide. *Sens Actuators B Chem* 2017;245:44–54. <https://doi.org/10.1016/j.snb.2017.01.106>.

[85] Zhang X, Bi X, Di W, Qin W. A simple and sensitive Ce(OH)CO₃/H₂O₂/TMB reaction system for colorimetric determination of H₂O₂ and glucose. *Sens Actuators B Chem* 2016;231:714–22. <https://doi.org/10.1016/j.snb.2016.03.087>.

[86] Lin L, Song X, Chen Y, Rong M, Zhao T, Wang Y, et al. Intrinsic peroxidase-like catalytic activity of nitrogen-doped graphene quantum dots and their application in the colorimetric detection of H₂O₂ and glucose. *Anal Chim Acta* 2015;869:89–95. <https://doi.org/10.1016/j.aca.2015.02.024>.

- [87] Hurdis EC, Romeyn Hendrik. Accuracy of Determination of Hydrogen Peroxide by Cerate Oxidimetry. *Anal Chem* 1954;26:320–5. <https://doi.org/10.1021/ac60086a016>.
- [88] Hanaoka S, Lin J-M, Yamada M. Chemiluminescent flow sensor for H₂O₂ based on the decomposition of H₂O₂ catalyzed by cobalt(II)-ethanolamine complex immobilized on resin. *Anal Chim Acta* 2001;426:57–64. [https://doi.org/10.1016/S0003-2670\(00\)01181-8](https://doi.org/10.1016/S0003-2670(00)01181-8).
- [89] Matsubara C, Kawamoto N, Takamura K. Oxo[5, 10, 15, 20-tetra(4-pyridyl)porphyrinato]titanium(IV): an ultra-high sensitivity spectrophotometric reagent for hydrogen peroxide. *The Analyst* 1992;117:1781. <https://doi.org/10.1039/an9921701781>.
- [90] Guascito MR, Filippo E, Malitesta C, Manno D, Serra A, Turco A. A new amperometric nanostructured sensor for the analytical determination of hydrogen peroxide. *Biosens Bioelectron* 2008;24:1057–63. <https://doi.org/10.1016/j.bios.2008.07.048>.
- [91] Rattu G, Khansili N, Maurya VK, Krishna PM. Lactate detection sensors for food, clinical and biological applications: a review. *Environ Chem Lett* 2021;19:1135–52. <https://doi.org/10.1007/s10311-020-01106-6>.
- [92] Kamel KS, Oh MS, Halperin ML. L-lactic acidosis: pathophysiology, classification, and causes; emphasis on biochemical and metabolic basis. *Kidney Int* 2020;97:75–88. <https://doi.org/10.1016/j.kint.2019.08.023>.
- [93] Rawoof SAA, Kumar PS, Vo D-VN, Devaraj K, Mani Y, Devaraj T, et al. Production of optically pure lactic acid by microbial fermentation: a review. *Environ Chem Lett* 2021;19:539–56. <https://doi.org/10.1007/s10311-020-01083-w>.
- [94] Dacko M, Lange T. Improved detection of lactate and β -hydroxybutyrate using MEGA-sLASER at 3 T. *NMR Biomed* 2019:e4100. <https://doi.org/10.1002/nbm.4100>.
- [95] Kim S, Kim K, Kim H-J, Lee H-N, Park TJ, Park YM. Non-enzymatic electrochemical lactate sensing by NiO and Ni(OH)₂ electrodes: A mechanistic

investigation. *Electrochimica Acta* 2018;276:240–6.
<https://doi.org/10.1016/j.electacta.2018.04.172>.

[96] Alam F, RoyChoudhury S, Jalal AH, Umasankar Y, Forouzanfar S, Akter N, et al. Lactate biosensing: The emerging point-of-care and personal health monitoring. *Biosens Bioelectron* 2018;117:818–29. <https://doi.org/10.1016/j.bios.2018.06.054>.

[97] Nalbandian M, Takeda M. Lactate as a Signaling Molecule That Regulates Exercise-Induced Adaptations. *Biology* 2016;5:38.
<https://doi.org/10.3390/biology5040038>.

[98] Jia W, Bandodkar AJ, Valdés-Ramírez G, Windmiller JR, Yang Z, Ramírez J, et al. Electrochemical Tattoo Biosensors for Real-Time Noninvasive Lactate Monitoring in Human Perspiration. *Anal Chem* 2013;85:6553–60.
<https://doi.org/10.1021/ac401573r>.

[99] Vaquer A, Barón E, De La Rica R. Wearable Analytical Platform with Enzyme-Modulated Dynamic Range for the Simultaneous Colorimetric Detection of Sweat Volume and Sweat Biomarkers. *ACS Sens* 2021;6:130–6.
<https://doi.org/10.1021/acssensors.0c01980>.

[100] Salata O. [No title found]. *J Nanobiotechnology* 2004;2:3.
<https://doi.org/10.1186/1477-3155-2-3>.

[101] Stark WJ. Nanoparticles in Biological Systems. *Angew Chem Int Ed* 2011;50:1242–58. <https://doi.org/10.1002/anie.200906684>.

[102] De M, Ghosh PS, Rotello VM. Applications of Nanoparticles in Biology. *Adv Mater* 2008;20:4225–41. <https://doi.org/10.1002/adma.200703183>.

[103] Yang Y-C, Wang Y-T, Tseng W-L. Amplified Peroxidase-Like Activity in Iron Oxide Nanoparticles Using Adenosine Monophosphate: Application to Urinary Protein Sensing. *ACS Appl Mater Interfaces* 2017;9:10069–77.
<https://doi.org/10.1021/acsami.6b15654>.

- [104] Sanfins E, Augustsson C, Dahlbäck B, Linse S, Cedervall T. Size-Dependent Effects of Nanoparticles on Enzymes in the Blood Coagulation Cascade. *Nano Lett* 2014;14:4736–44. <https://doi.org/10.1021/nl501863u>.
- [105] Bai Y, Dou Y, Xie L-H, Rutledge W, Li J-R, Zhou H-C. Zr-based metal–organic frameworks: design, synthesis, structure, and applications. *Chem Soc Rev* 2016;45:2327–67. <https://doi.org/10.1039/C5CS00837A>.
- [106] Li T, Hu P, Li J, Huang P, Tong W, Gao C. Enhanced peroxidase-like activity of Fe@PCN-224 nanoparticles and their applications for detection of H₂O₂ and glucose. *Colloids Surf Physicochem Eng Asp* 2019;577:456–63. <https://doi.org/10.1016/j.colsurfa.2019.06.012>.
- [107] Fu S, Wang S, Zhang X, Qi A, Liu Z, Yu X, et al. Structural effect of Fe₃O₄ nanoparticles on peroxidase-like activity for cancer therapy. *Colloids Surf B Biointerfaces* 2017;154:239–45. <https://doi.org/10.1016/j.colsurfb.2017.03.038>.
- [108] Bao Y-W, Hua X-W, Ran H-H, Zeng J, Wu F-G. Metal-doped carbon nanoparticles with intrinsic peroxidase-like activity for colorimetric detection of H₂O₂ and glucose. *J Mater Chem B* 2019;7:296–304. <https://doi.org/10.1039/C8TB02404A>.
- [109] Kaushik A, Khan R, Solanki PR, Pandey P, Alam J, Ahmad S, et al. Iron oxide nanoparticles–chitosan composite based glucose biosensor. *Biosens Bioelectron* 2008;24:676–83. <https://doi.org/10.1016/j.bios.2008.06.032>.
- [110] Castro GR, Nadda AK, Nguyen TA, Qi X, Yasin G. *Nanomaterials for Biocatalysis*. Elsevier Science; 2021.
- [111] Gao L, Zhuang J, Nie L, Zhang J, Zhang Y, Gu N, et al. Intrinsic peroxidase-like activity of ferromagnetic nanoparticles. *Nat Nanotechnol* 2007;2:577–83. <https://doi.org/10.1038/nnano.2007.260>.
- [112] Fu Z, Zeng W, Cai S, Li H, Ding J, Wang C, et al. Porous Au@Pt nanoparticles with superior peroxidase-like activity for colorimetric detection of spike protein of SARS-CoV-2. *J Colloid Interface Sci* 2021;604:113–21. <https://doi.org/10.1016/j.jcis.2021.06.170>.

- [113] Otto M. *Chemometrics: statistics and computer application in analytical chemistry*. Third edition. Weinheim: Wiley-VCH Verlag GmbH & Co. KGaA; 2017.
- [114] Peer M, Sarig R. Color change in teeth due to burning: Spectrophotometric analysis. *Forensic Sci Int* 2023;345:111608. <https://doi.org/10.1016/j.forsciint.2023.111608>.
- [115] De Carvalho Oliveira G, Machado CCS, Inácio DK, Silveira Petrucci JFD, Silva SG. RGB color sensor for colorimetric determinations: Evaluation and quantitative analysis of colored liquid samples. *Talanta* 2022;241:123244. <https://doi.org/10.1016/j.talanta.2022.123244>.
- [116] Badar F, Dean LT, Loy J, Redmond M, Vandi L-J, Novak JI. Preliminary color characterization of HP Multi Jet Fusion additive manufacturing with different orientations and surface finish. *Rapid Prototyp J* 2023;29:582–93. <https://doi.org/10.1108/RPJ-04-2022-0136>.
- [117] Yang R, Cheng W, Chen X, Qian Q, Zhang Q, Pan Y, et al. Color Space Transformation-Based Smartphone Algorithm for Colorimetric Urinalysis. *ACS Omega* 2018;3:12141–6. <https://doi.org/10.1021/acsomega.8b01270>.
- [118] Şen M, Yüzer E, Doğan V, Avcı İ, Ensarioğlu K, Aykaç A, et al. Colorimetric detection of H₂O₂ with Fe₃O₄@Chi nanozyme modified µPADs using artificial intelligence. *Microchim Acta* 2022;189:373. <https://doi.org/10.1007/s00604-022-05474-4>.
- [119] Ayres LB, Gomez FJV, Linton JR, Silva MF, Garcia CD. Taking the leap between analytical chemistry and artificial intelligence: A tutorial review. *Anal Chim Acta* 2021;1161:338403. <https://doi.org/10.1016/j.aca.2021.338403>.
- [120] Doğan V, Yüzer E, Kılıç V, Şen M. Non-enzymatic colorimetric detection of hydrogen peroxide using a µPAD coupled with a machine learning-based smartphone app. *The Analyst* 2021;146:7336–44. <https://doi.org/10.1039/D1AN01888D>.
- [121] Duan S, Cai T, Zhu J, Yang X, Lim EG, Huang K, et al. Deep learning-assisted ultra-accurate smartphone testing of paper-based colorimetric ELISA assays. *Anal Chim Acta* 2023;1248:340868. <https://doi.org/10.1016/j.aca.2023.340868>.

- [122] Kılıç V, Mercan ÖB, Tetik M, Kap Ö, Horzum N. Non-enzymatic colorimetric glucose detection based on Au/Ag nanoparticles using smartphone and machine learning. *Anal Sci* 2022;38:347–58. <https://doi.org/10.2116/analsci.21P253>.
- [123] Mercan OB, Dogan V, Kilic V. Time Series Analysis based Machine Learning Classification for Blood Sugar Levels. 2020 Med. Technol. Congr. TIPTEKNO, Antalya: IEEE; 2020, p. 1–4. <https://doi.org/10.1109/TIPTEKNO50054.2020.9299279>.
- [124] Mohammadi A, Barikani M. Synthesis and characterization of superparamagnetic Fe₃O₄ nanoparticles coated with thiodiglycol. *Mater Charact* 2014;90:88–93. <https://doi.org/10.1016/j.matchar.2014.01.021>.
- [125] Srivastava M, Singh J, Yashpal M, Gupta DK, Mishra RK, Tripathi S, et al. Synthesis of superparamagnetic bare Fe₃O₄ nanostructures and core/shell (Fe₃O₄/alginate) nanocomposites. *Carbohydr Polym* 2012;89:821–9. <https://doi.org/10.1016/j.carbpol.2012.04.016>.
- [126] Li S, Zhang T, Tang R, Qiu H, Wang C, Zhou Z. Solvothermal synthesis and characterization of monodisperse superparamagnetic iron oxide nanoparticles. *J Magn Mater* 2015;379:226–31. <https://doi.org/10.1016/j.jmmm.2014.12.054>.
- [127] Cao S-L, Li X-H, Lou W-Y, Zong M-H. Preparation of a novel magnetic cellulose nanocrystal and its efficient use for enzyme immobilization. *J Mater Chem B* 2014;2:5522–30. <https://doi.org/10.1039/C4TB00584H>.
- [128] Ragavan KV, Ahmed SR, Weng X, Neethirajan S. Chitosan as a peroxidase mimic: Paper based sensor for the detection of hydrogen peroxide. *Sens Actuators B Chem* 2018;272:8–13. <https://doi.org/10.1016/j.snb.2018.05.142>.
- [129] Mucha M, Pawlak A. Complex study on chitosan degradability. *Polimery* 2002;47:509–16. <https://doi.org/10.14314/polimery.2002.509>.
- [130] Fan Z, Xu Y, Zhang D. Local Linear Discriminant Analysis Framework Using Sample Neighbors. *IEEE Trans Neural Netw* 2011;22:1119–32. <https://doi.org/10.1109/TNN.2011.2152852>.

- [131] Tharwat A, Gaber T, Ibrahim A, Hassanien AE. Linear discriminant analysis: A detailed tutorial. *AI Commun* 2017;30:169–90. <https://doi.org/10.3233/AIC-170729>.
- [132] Chicco D, Jurman G. The advantages of the Matthews correlation coefficient (MCC) over F1 score and accuracy in binary classification evaluation. *BMC Genomics* 2020;21:6. <https://doi.org/10.1186/s12864-019-6413-7>.
- [133] Tian J, Liu Y, Zheng W, Yin L. Smog prediction based on the deep belief - BP neural network model (DBN-BP). *Urban Clim* 2022;41:101078. <https://doi.org/10.1016/j.uclim.2021.101078>.
- [134] Verma S, Choudhary J, Singh KP, Chandra P, Singh SP. Uricase grafted nanoconducting matrix based electrochemical biosensor for ultrafast uric acid detection in human serum samples. *Int J Biol Macromol* 2019;130:333–41. <https://doi.org/10.1016/j.ijbiomac.2019.02.121>.
- [135] Guo X, Wang Y, Wu F, Ni Y, Kokot S. A colorimetric method of analysis for trace amounts of hydrogen peroxide with the use of the nano-properties of molybdenum disulfide. *The Analyst* 2015;140:1119–26. <https://doi.org/10.1039/C4AN01950D>.
- [136] Ostovan A, Arabi M, Wang Y, Li J, Li B, Wang X, et al. Greenificated Molecularly Imprinted Materials for Advanced Applications. *Adv Mater* 2022;34:2203154. <https://doi.org/10.1002/adma.202203154>.
- [137] Riaz MA, Chen Y. Electrodes and electrocatalysts for electrochemical hydrogen peroxide sensors: a review of design strategies. *Nanoscale Horiz* 2022;7:463–79. <https://doi.org/10.1039/D2NH00006G>.
- [138] Caporali S, Bardi U. Corrosion Mechanism in Artificial Sweat Solution of In-Bearing White Bronze Alloy. *CORROSION* 2012;68:025001-1-025001–8. <https://doi.org/10.5006/1.3683223>.
- [139] Mohamed SA, Abulnaja KO, Ads AS, Khan JA, Kumosani TA. Characterisation of an anionic peroxidase from horseradish cv. Balady. *Food Chem* 2011;128:725–30. <https://doi.org/10.1016/j.foodchem.2011.03.096>.

- [140] Xu P, Yano T, Yamamoto K, Suzuki H, Kumagai H. Characterization of a lactate oxidase from a strain of gram negative bacterium from soil. *Appl Biochem Biotechnol* 1996;56:277–88. <https://doi.org/10.1007/BF02786958>.
- [141] Kiliç V. Yapay Zeka Tabanlı Akıllı Telefon Uygulaması ile Kan Şekeri Tahmini. *Eur J Sci Technol* 2021. <https://doi.org/10.31590/ejosat.950914>.
- [142] Palaz Z, Doğan V, Kiliç V. Smartphone-based Multi-parametric Glucose Prediction using Recurrent Neural Networks. *Eur J Sci Technol* 2022. <https://doi.org/10.31590/ejosat.1041547>.
- [143] Palsson B, Sveinsson JR, Ulfarsson MO. Blind Hyperspectral Unmixing Using Autoencoders: A Critical Comparison. *IEEE J Sel Top Appl Earth Obs Remote Sens* 2022;15:1340–72. <https://doi.org/10.1109/JSTARS.2021.3140154>.
- [144] Ghali R, Akhloufi MA, Mseddi WS. Deep Learning and Transformer Approaches for UAV-Based Wildfire Detection and Segmentation. *Sensors* 2022;22:1977. <https://doi.org/10.3390/s22051977>.
- [145] Bhupendra, Moses K, Miglani A, Kumar Kankar P. Deep CNN-based damage classification of milled rice grains using a high-magnification image dataset. *Comput Electron Agric* 2022;195:106811. <https://doi.org/10.1016/j.compag.2022.106811>.
- [146] Sun J, Liu X, Mei X, Zhao J, Plumbley MD, Kiliç V, et al. Deep Neural Decision Forest for Acoustic Scene Classification 2022. <https://doi.org/10.48550/ARXIV.2203.03436>.
- [147] Chang J, Lu Y, Xue P, Xu Y, Wei Z. ACP: Automatic Channel Pruning via Clustering and Swarm Intelligence Optimization for CNN 2021. <https://doi.org/10.48550/ARXIV.2101.06407>.
- [148] Wang N, Wang Y, Er MJ. Review on deep learning techniques for marine object recognition: Architectures and algorithms. *Control Eng Pract* 2022;118:104458. <https://doi.org/10.1016/j.conengprac.2020.104458>.
- [149] Samadi Pakchin P, Ghanbari H, Saber R, Omidi Y. Electrochemical immunosensor based on chitosan-gold nanoparticle/carbon nanotube as a platform and

lactate oxidase as a label for detection of CA125 oncomarker. *Biosens Bioelectron* 2018;122:68–74. <https://doi.org/10.1016/j.bios.2018.09.016>.

Appendices

Appendix A

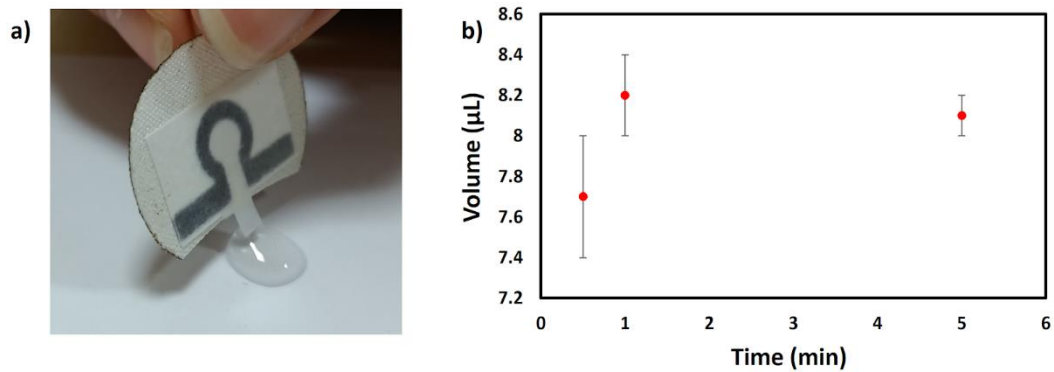


Figure A. 1: An image showing a patch used for fluid absorption testing (a). The variation in volume of fluid absorbed by different patches over time (b).

Patch fluid absorption

A number of patches were prepared as shown in Figure A.1a to absorb liquid properly from a droplet. Briefly, 100 μL of dH_2O was put on a weighing boat and weighted using a sensitive analytical balance (Radwag, Poland). Next, a patch was dipped into the droplet for 30 sec and the remaining fluid was weighted again to calculate the volume absorbed by the patch. The process was repeated in the same way for 1 and 5 min, respectively.

Appendix B

Publications from the Thesis

Journal Articles

1. **Yüzer, E.**, Doğan, V., Kılıç, V., & Şen, M. (2022), Smartphone embedded deep learning approach for highly accurate and automated colorimetric lactate analysis in sweat. *Sensors and Actuators B: Chemical*, 371, 132489.
2. Şen, M., **Yüzer, E.**, Doğan, V., Avcı, İ., Ensarioğlu, K., Aykaç, A., ... & Kılıç, V. (2022). Colorimetric detection of H₂O₂ with Fe₃O₄@ Chi nanozyme modified μ PADs using artificial intelligence. *Microchimica Acta*, 189(10), 373.

Curriculum Vitae

Name Surname : Elif Yüzer

Education:

2016–2021 İzmir Kâtip Çelebi University, Dept. of Biomedical Eng.

2021–2023 İzmir Kâtip Çelebi University, Dept. of Biomedical Eng. (MSc.)

Work Experience:

2021-2022 Biomedical Engineer Intern

2022 – 2023 Research Project Scholar -Tubitak 1001

Publications :

1. Doğan, V., **Yüzer, E.**, Kılıç, V., & Şen, M. (2021). Non-enzymatic colorimetric detection of hydrogen peroxide using a μ PAD coupled with a machine learning-based smartphone app. *Analyst*, *146*(23), 7336-7344.
2. Şen, M., **Yüzer, E.**, Doğan, V., Avcı, İ., Ensarioğlu, K., Aykaç, A., ... & Kılıç, V. (2022). Colorimetric detection of H₂O₂ with Fe₃O₄@ Chi nanozyme modified μ PADs using artificial intelligence. *Microchimica Acta*, *189*(10), 373.
3. **Yüzer, E.**, Doğan, V., Kılıç, V., & Şen, M. (2022). Smartphone embedded deep learning approach for highly accurate and automated colorimetric lactate analysis in sweat. *Sensors and Actuators B: Chemical*, *371*, 132489.